**Defense Threat Reduction Agency**
**8725 John J. Kingman Road, MS**
**6201 Fort Belvoir, VA 22060-6201**

**DTRA-TR-21-36**

TECHNICAL REPORT

# Impact of Radiation on Pattern Recognition in Memristor-Based Neuromorphic Circuits



May 2021

HDTRA1-17-1-0036

Prepared by: Kurtis Cantley

Boise State University
Boise, ID 83725

# REPORT DOCUMENTATION PAGE

*Form Approved*
*OMB No. 0704-0188*



| 1. REPORT DATE *(DD-MM-YYYY)* | 2. REPORT TYPE | 3. DATES COVERED *(From - To)* |
|---|---|---|
| 03/31/2021 | Final Report | 4/10/2017 - 12/31/2021 |

**4. TITLE AND SUBTITLE**
Impact of Radiation on Pattern Recognition in Memristor-Based Neuromorphic Circuits

**5a. CONTRACT NUMBER**

**5b. GRANT NUMBER**
HDTRA1-17-1-0036

**5c. PROGRAM ELEMENT NUMBER**

**6. AUTHOR(S)**
Kurtis D. Cantley

**5d. PROJECT NUMBER**
J9BAP723184

**5e. TASK NUMBER**

**5f. WORK UNIT NUMBER**

**7. PERFORMING ORGANIZATION NAME(S) AND ADDRESS(ES)**
Boise State University
1910 University Drive
Boise, ID 83725

**8. PERFORMING ORGANIZATION REPORT NUMBER**

**9. SPONSORING/MONITORING AGENCY NAME(S) AND ADDRESS(ES)**
Defense Threat Reduction Agency
8725 John J. Kingman Road
Fort Belvoir, VA 22060-6201

**10. SPONSOR/MONITOR'S ACRONYM(S)**
DTRA

**11. SPONSOR/MONITOR'S REPORT NUMBER(S)**

**12. DISTRIBUTION/AVAILABILITY STATEMENT**

**13. SUPPLEMENTARY NOTES**

**14. ABSTRACT**

By the nature of their dense interconnectivity, future electronic spiking neural networks (SNNs) have the potential to be extraordinarily robust and defect-tolerant, in addition to energy-efficient. In this research, the effects on SNNs of high levels of radiation generated by weapons of mass destruction is explored through advanced modeling and simulation. Effects of this radiation on the spike timing-dependent plasticity learning rule, system stability, and pattern learning ability of the spiking neural network are analyzed.

**15. SUBJECT TERMS**
Spiking neural networks, weapons of mass destruction, radiation, spike timing-dependent plasticity, memristors

| 16. SECURITY CLASSIFICATION OF: | | | 17. LIMITATION OF ABSTRACT | 18. NUMBER OF PAGES | 19a. NAME OF RESPONSIBLE PERSON |
|---|---|---|---|---|---|
| a. REPORT | b. ABSTRACT | c. THIS PAGE | | | Jacob A. Calkins |
| | | | | | 19b. TELEPHONE NUMBER *(Include area code)* 571-616-5946 |

# DTRA Basic Research Final Report

**Grant/Award #:** HDTRA1-17-1-0036

**PI Name:** Kurtis D. Cantley

**Organization/Institution:** Boise State University

**Project Title:** Impact of Radiation on Pattern Recognition in Memristor-Based Neuromorphic Circuits

## Table of Contents

## List of Figures

## Abbreviations

ISI – Inter-Spike Interval

LIF – Leaky Integrate-and-Fire

MSE – Mean Squared Error

MOSFET – Metal Oxide Semiconductor Field-Effect Transistor

OCR – Optical Character Recognition

ReRAM – Resistive Random Access Memory

SNN – Spiking Neural Network

SPICE – Simulation Program with Integrated Circuit Emphasis

STDP – Spike Timing-Dependent Plasticity

STPR – Spatio-Temporal Pattern Recognition

WMD – Weapon of Mass Destruction

## Executive Summary

By the nature of their dense interconnectivity, future electronic spiking neural networks (SNNs) have the potential to be extraordinarily robust and defect-tolerant, in addition to energy-efficient. In this research, the effects on SNNs of high levels of radiation generated by weapons of mass destruction is explored through advanced modeling and simulation. The networks are designed and trained to recognize spatio-temporal patterns representing characters in the alphabet. Two-terminal resistive memory devices (memristors) are used as synapses to manipulate conductivity paths in the network. Spike-timing-dependent plasticity (STDP) learning behavior results in pattern learning and is achieved using biphasic shaped pre- and post-synaptic spikes. A $TiO_2$ based non-linear drift memristor model designed in Verilog-A is used to implement synaptic behavior and is modified to include experimentally observed effects of state-altering, ionizing, and off-state degrading radiation on the device. Effects of this radiation on the STDP learning rule, system stability, and pattern learning ability of the spiking neural network are simulated.

In general, radiation interaction events distort the STDP learning curve undesirably, making the connection between afferents stronger by increasing the overall conductance of synapses. At lower radiation flux intensities of shorter duration, the network is often able to recover and fully relearn the pattern with consistent training. As the radiation flux and duration increases, it can overwhelm the leaky integrate-and-fire (LIF) post-synaptic neuron circuit and cause stability issues and/or failure to relearn the pattern. Most often, this implies that some number of pixels in the learned pattern were significantly distorted compared to the training pattern. In the total absence of repetitive pattern presentation, the radiation effects accumulate in the system and it never regains stability. The results suggest that having the ability to retrain networks (even to a moderate degree) after they have been deployed for inference tasks would dramatically increase resilience of these systems.

The impact of neuron “death” (neuron circuit failure) due to radiation is also studied in this work using a similar SNN spatio-temporal pattern approach. The simulations observe the effect on the learning ability of the network for three general cases: when only neurons that participate in patterns were disabled, when only non-participating neurons were disabled, or when non-selective neuron death occurred randomly after initial training (the most realistic scenario). As expected, the network learning ability was least affected in the case when the non-participating afferents were disabled selectively. In this situation, the network often shows the capacity to recover even with loss of 25% of the non-participating afferents. When non-selective neuron death occurred, the pattern learning ability degraded rapidly for the case where death occurred simultaneously (such as from a very high flux but short duration radiation event). However, gradual neuron death causes far less deterioration in the network’s ability to recognize patterns. In fact, minimal degradation even with loss of 25% of the afferents was observed in some simulations. These results suggest that non-participating afferents can contribute to improving the learning ability of the network. Some network topologies may also be naturally more resilient than others. Additional research will be required to address that possibility at a more detailed level.

# 1. Introduction

The human brain can process thousands of streams of information simultaneously using very little energy, while its versatility and ability to learn is key to cognition and intelligence [1], [2]. The brain consists of more than 100 billion neurons, each connected to thousands of other neurons via synapses [3], [4]. Currently, it is impossible to model or perform real-time simulation of the human brain. In part, this is due to our incomplete understanding of its operation, but also because computing technology is not advanced enough to capture the appropriate level of complexity. However, researchers are working to mimic the behavior of large-scale biological neural networks using electronics to open up the possibility of creating artificial intelligence. In doing so, the hope is to capture other desirable features simultaneously, such as the brain's extreme tolerance to defects and adaptability. This report outlines a research effort to investigate the defect tolerance of future ***spiking neural network (SNN)*** implementations using memristive synapses.

## 1.1 Project Goals and Timeline

The specific goal of this research is to explore the effects of radiation generated by ***weapons of mass destruction (WMDs)*** on future electronic SNNs. These neuromorphic architectures are able to perform many computational tasks more efficiently than today's digital systems. Due to their high degree of interconnectivity and adaptability, they are also expected to be more robust than digital electronics overall, even though they are constructed with many of the same types of devices. A main outcome of this research is to quantify the degree to which radiation exposure alters pattern recognition accuracy and performance of neuromorphic circuits with memristive synapses. Two tasks on which we will focus are ***spatio-temporal pattern recognition (STPR)*** with unsupervised, spike timing-dependent learning and ***optical character recognition (OCR)*** through supervised training. A second outcome is investigating new designs or alterations to current approaches that could mitigate any threats to these systems posed by radiation.

Executing this project requires development of ***SPICE (Simulation Program with Integrated Circuit Emphasis)*** device models for the constituent components (particularly the memristors) that accurately capture the effects of radiation. It also requires estimates as to the of radiation interactions on the devices and system over time, which in turn is a function of the operating environment and specific WMD threat. A brief description of the main tasks from the original research proposal are outlined below, grouped by the year in which they were scheduled to begin. Most of these tasks were executed as stated with very little change, although a few were altered slightly.

***Year #1***

Task 1: Examine WMD radiation exposure profiles (functions of time and spatial position) in terms of the types and amounts of radiation produced by nuclear and radiological WMDs.

Task 2: Study radiation effects in memristive devices comprised of many different types of materials with different structures and electrical characteristics.

Task 3: Update memristor SPICE to capture the wide variety of observed memristor behaviors and subsequent complex characteristics when exposed to radiation.

Task 4: Implement models for radiation in transistors. This was eventually updated to include overall neuron circuit effects instead of the individual transistor level.

***Year #2***

Task 5: Generate circuit designs and layouts so that cross-sectional interaction probability of radioactive particles can be calculated.

Task 6: Determine statistical radiation exposure for generated layouts using cross-sectional areas (layouts in Task 5) and typical WMD radiation profiles (Task 1).

Task 7: Spatio-temporal pattern recognition simulation and analysis of training time, network stability, successful pattern detection probability, and false positive frequency.

***Year #3***

Task 8: Optical character recognition simulation and analysis using the Mixed National Institute of Standards and Technology (MNIST) handwriting database and a trained network.

Task 9: Consider network designs to mitigate threats to neural network performance posed by radiation.

The original timeline for carrying out and completing the tasks outlined above is shown in the Gantt chart of Figure 1.1. A no-cost extension through the end of the 2020 calendar year was also approved for this project (total duration of 3.5 years). None of the tasks are directly linked because they are not necessarily required to be performed consecutively. Many can be performed in parallel with some flexibility depending on the skillset of students working on the project. For instance, neuron circuit design, layout, and simulation was previously completed ahead of schedule. However, determining appropriate radiation profiles and robust statistical calculation of exposure given circuit designs and layouts is ongoing and has presented a significant challenge. Simulation of STPR and OCR has commenced without full understanding of radiation effects and completely accurate interaction probabilities, which can be updated over time.

| ID | Task Name | Start | Finish | Duration |
|---|---|---|---|---|
| 1 | WMD Radiation Exposure Profiles | 1/2/2017 | 3/31/2017 | 65d |
| 2 | Radiation Effects in Memristors | 3/1/2017 | 8/30/2017 | 131d |
| 3 | Update Memristor SPICE Models | 2/2/2017 | 12/29/2017 | 237d |
| 4 | Model Radiation in Transistors | 6/15/2017 | 3/15/2018 | 196d |
| 5 | Generate Circuit Designs and Layouts | 1/2/2018 | 8/30/2018 | 173d |
| 6 | Statistically Determine Radiation Exposure | 1/1/2018 | 12/28/2018 | 260d |
| 7 | STPR Simulation and Analysis | 11/1/2018 | 8/30/2019 | 217d |
| 8 | OCR Simulation and Analysis | 1/1/2019 | 12/31/2019 | 261d |
| 9 | Network Designs to Mitigate Threat | 11/1/2018 | 12/27/2019 | 302d |
| 10 | Compile Summary of Results | 11/1/2019 | 12/31/2019 | 43d |

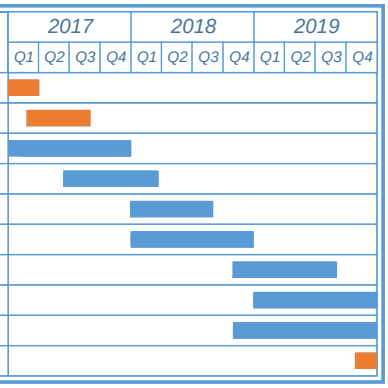


**Figure 1.1.** Original proposal Gantt chart showing organization and timeline of research tasks.

## 1.2 Summary of Outcomes by Year

***Year #1***

The primary accomplishment in the first year was development of a memristor behavioral model that captures radiation interactions (Verilog-A code provided in Appendix A). In this effort, the team completed tasks 2 and 3. Neuron circuit designs and layouts were also finished ahead of schedule, and work begun on tasks 1, 4, and 6. Later, task 6 morphed into a more appropriate approach in which radiation effects were captured at the neuron circuit level (due to a disabled transistor or capacitor) versus at the transistor level. Basic network simulations (without pattern encoding) were also initiated the first year.

***Year #2***

Much more extensive network-level simulations were carried out in the second year of the project. The encoding and training scheme for STPR and OCR was implemented, and radiation profiles were

also included using the memristor behavioral model. For tasks 5 and 6, it was determined that the area of the metal-insulator-metal (MIM) capacitors dominate most neuron circuit designs. Thus, radiation interactions have a much higher probability of causing defects in the insulator and shorting out these devices, thereby disabling the neuron circuit.

***Year #3***

In the third year of this project, the main focus of the team was continuing to analyze network performance when subjected to radiation interactions occurring at the synapses. However, we also began exploring degradation mechanisms that would cause neurons to cease operation (neuron death). In this effort, the team made outstanding progress on tasks 4, 7, and 8.

## 1.3 Significant Achievements

A number of significant achievements were realized over the duration of this 3.5-year project. These are summarized below:

- Two articles submitted to peer-reviewed journals directly involving this work (one accepted, another currently under review), with a third article indirectly related.
- Four total conference proceedings published (one invited).
- Student best poster award at the International Conference on Neuromorphic Systems (ICONS) 2019.
- Funded student Sumedha Gandharava Dahl received PhD in Summer 2020 and is currently employed at Micron Technology.

## 2. Device and Circuit Modeling

### 2.1 Memristor Model Characteristics

The literature shows that extensive effort has been made to physically implement memristors, and significant progress has been made in modeling these devices as well [5], [6], [15]–[19], [7]–[14]. Modeling not only helps better understand the working principals and the performance of the device, but also facilitates simulation of the devices in larger and more complicated circuits. One challenge in implementing good memristor models is the often non-deterministic behavior of the devices. The presently available models in the literature can be categorized into either physical or mathematical models. The mathematical SPICE models like TEAM [15], Simmons Tunneling [17] and Yakopcic [16] have a minimal (if any) physical explanation for the relatively large number of input parameters used (up to 13). These mathematical models have many parameters to adjust, and can therefore match respective device characteristics very closely, but their general accuracy is limited. It is thus difficult to use pulse shaping reliably because the input parameters need to be modified for each given shape and frequency of the input [16], [17], [20]. On the other hand, most of the physical memristor models presented in literature depend on the ionic drift behavior for $TiO_2$ memristive devices presented by Strukov [5]. This subsection discusses and presents the simulation results of the $TiO_2$ based non-linear ionic drift memristor model, for which the characteristics are published in [21].

Many models are studied in the literature, the most explored ones being the linear ion drift model by Strukov et al. [5], the non-linear ion drift model by Laiho et al. [22], the Simmons tunneling barrier model by Pickett [18], the Yakopcic model by Yakopcic et al. [23], and the TEAM model by Kvatinsky et al. [15]. Both the linear and the nonlinear drift models are based on the theory that memristors are represented by a circuit with two resistors, the high resistance coming from the non-conductive (oxide) region and the low resistance from the conductive region. The Laiho's non-linear drift model assumes non-linear dependencies between the voltage and the state variable ($\frac{w}{D}$), which is a normalized parameter. The Simmons model assumes that the ions in the devices present exponential dependence, resulting in the model's exponential and symmetric switching behavior between the current and the state variable. The TEAM model assumes polynomial dependence between the memristor current and the state variable. Other models are also presented in the literature for self-directed channel devices [24], where an empirical approach is used to match the device I-V characteristics [25].

This work uses a $TiO_2$ based ionic drift memristor model. The model simulations are a close representation of oxide-based device characteristics at multiple frequencies, pulse shapes, and sizes. Another reason for the use of this model is because multiple radiation studies have been performed on the $TiO_2$ memristive devices [26]–[28]. The model is also voltage controlled, has an explicit I-V relationship, includes non-linearity, has a normalized state variable ($\frac{w}{D}$), and the model is not purely mathematical. The model has lower accuracy, but has been widely used in simulations and comparison studies like Chua et al. for designing memristor bridge synapse base neural networks and by other references [16], [29]–[33].

The memristor models are accompanied by a window function that is used to add non-linearity to the model, which is specific to the device. The window function also forces the physical boundary ($0 \leq \frac{w}{D} \leq 1$) of the device in the model. Multiple window functions compatible with the ion-drift model are used in the literature by Joglekar and Wolf [34], Biolek et al. [35], Prodromakis et al. [33], and piecewise by Yu at al. [36]. All of the window functions can induce non-linear drift in the model and can only provide symmetrical window functions (except the piecewise function which could induce

asymmetry). The $TiO_2$ based non-linear ionic drift memristor model was proposed by Strukov et al. in 2008 [5]. Since then, the model has been widely adopted in the literature, and has been used extensively in simulations and comparison studies, like Chua et al., for designing memristor bridge synapse base neural networks [16], [29]–[33].

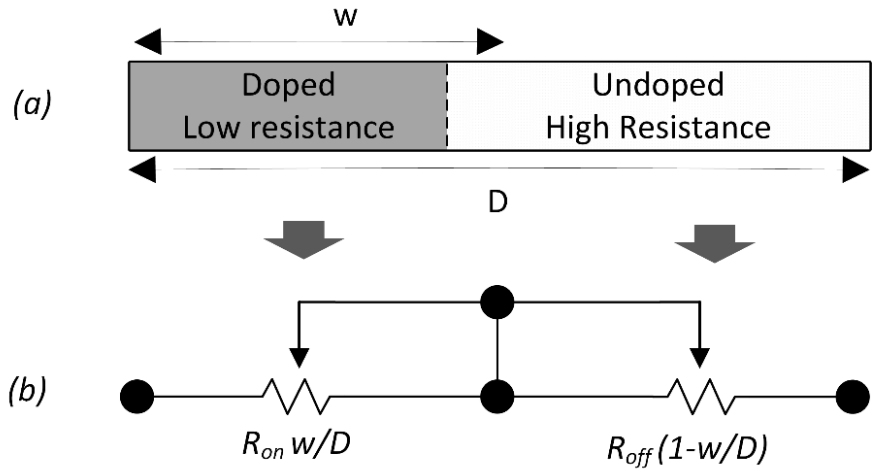


**Figure 2.1.** Representation of a memristor as suggested by Strukov. (a) Memristive device of thickness "D" represented as a combination of doped (low resistance) and undoped (high resistance) region. (b) Circuit representation of two variable resistors, $R_{on}$ (less resistive region of width w) and $R_{off}$ (high resistive region of width, D−w) [5].

The ionic drift model effectively treats the instantaneous total resistance of a memristive device $R_{mem}$ as two variable resistors connected in series, as represented in Figure. One of these resistors represents a conductive region of thickness w inside a device with physical thickness D. The other resistor corresponds to a less conductive region of thickness D−w (Figure 2.1a). When w is almost equal to the device thickness, D, the device is in its lowest resistance state, with the resistance value $R_{mem}$ equal to $R_{on}$. The device is in a high resistance state, with $R_{mem}$ equal to $R_{off}$, when w is much less than the total device thickness D.

The total resistance of this memristive device is called the memristance ($R_{mem}$) and has units of Ohms. The I-V relationship of the two variable resistance system represented in Figureb can be given by Ohm's Law, where $R_{mem}$ is a state-dependent resistance. Thus, the memristance can be written mathematically as:

$$R_{mem} = R_{on}\frac{w}{D} + R_{off}\left(1 - \frac{w}{D}\right) = R_{off} - (R_{off} - R_{on})\frac{w}{D} \qquad (2.1)$$

From Equation (2.1) at $w \approx D$, then $R_{mem} \approx R_{on}$ (low resistance state) and at $w \approx 0$, $R_{mem} \approx R_{off}$ (high resistance state). The ratio $\frac{w}{D}$ is referred to as the state variable of the device and is physically bounded $0 < \frac{w}{D} < 1$, with 0 being the most resistive state and 1 being the most conductive state. Change in the state variable is a function of time and depends on the mobility of dopant ions ($\mu$) drifting under a uniformly applied electric field as:

$$\frac{dw}{dt} = \frac{R_{on}\,\mu}{D} I_{mem} \qquad (2.2)$$

In Equation (2.2), $\frac{R_{on}}{D} I_{mem}$, is the electric field in the conductive region of length w. The equivalent circuit, as suggested by Biolek et al. [35], is represented in Figure a and consists of dependent voltage source $E_{mem}$ and resistance $R_{off}$ in series. Thus, the circuit equation is:

$$V_{mem} = R_{mem} I_{mem} = R_{off} I_{mem} + E_{mem} \qquad (2.3)$$

Comparing Equation (2.1) and Equation (2.3):

$$E_{mem} = -I_{mem}(R_{off} - R_{on})\frac{w}{D} \qquad (2.4)$$

Equation (2.4) shows that $E_{mem}$ is a dependent voltage source that is controlled by the state variable ($\frac{w}{D}$) of the device (from the auxiliary circuit in Figure b) and, current ($I_{mem}$) at a given time.

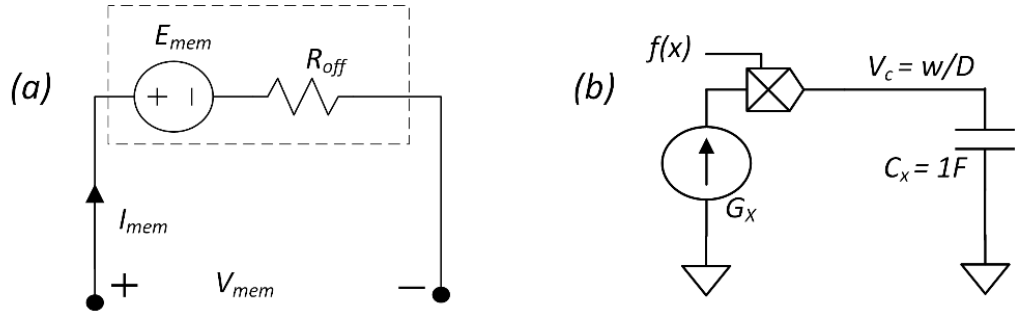


**Figure 2.2.** Schematic representation of the memristor model as suggested by Biolek [35]. (a) Implementation of the memristive circuit with dependent source $E_{mem}$ and resistance $R_{off}$. (b) Auxiliary circuit with $I_{mem}$ dependent current source $G_x$ and 1F capacitor $C_x$. The voltage across $C_x$ controls $E_{mem}$.

The auxiliary circuit, shown in Figure b, which sources $E_{mem}$, contains a dependent current source $G_x$ connected to a large 1 F capacitor ($C_x$). The voltage across the capacitor $C_x$ feeds the $E_{mem}$ in the memristor circuit shown in Figure a. $I_{mem}$ drives the current source ($G_x$) as:

$$G_x = \frac{R_{on}\,\mu\, I_{mem}}{D^2} \qquad (2.5)$$

Thus, using the relation $I = C\,\frac{dV}{dt}$ we get,

$$\frac{dV_c}{dt} = G_x\, f(x), \qquad \text{if } 0 < \frac{w}{D} < 1,\ f(x) = 1 \quad \text{else, } f(x) = 0 \qquad (2.6)$$

where f(x) is the window function which introduces non-linearity in the device.

In Figure b, the current source is multiplied by the window function, f(x). This window function handles the non-linear dopant drift in w when it is near the physical boundaries, which occur when $\frac{w}{D}$ ≈0 or $\frac{w}{D}$ ≈1. It also helps keep $\frac{w}{D}$ bounded in the appropriate range between 0 and 1. The window function used in this work is from Jogelkar and Wolf [34] and is given as:

$$f(x) = 1 - (2x - 1)^8 \qquad (2.7)$$

Thus, using the relation, $I = C\,\frac{dV}{dt}$, we get:

$$\frac{dV_c}{dt} = G_x\, f(x) \qquad (2.8)$$

The window function in Equation (2.7) is symmetric about zero voltage, but different window functions can be used, that change depending on the polarity of the applied voltage, to model asymmetry in the I-V characteristics [16]. Other parameters used in the model are $R_{on}$ = 10 kΩ, $R_{off}$ = 100 kΩ (when not changing due to radiation), $\mu = 10\ fm^2/V$ and D = 10 nm, so as to mimic the characteristics of the HP Labs memristor as estimated in [35].

The memristor behavioral model is implemented in Verilog-A (Appendix A.1) and the simulations are done using Cadence Virtuoso Spectre. Figure a shows the simulated current versus voltage characteristics of the model. The plot displays all of the three characteristic fingerprints of a memristor [52], [55], [60]. The hysteresis curve is pinched at the center, the area of the hysteresis is decreasing with increasing frequency, and finally, it ends in a straight line at higher frequencies of 100 Hz and 1 kHz. These results demonstrate the same results from the ionic memristor model with window function represented by Equation (2.7). In this case, the memristor model has no threshold, thus, even at smaller voltages the device forces the change in the conductivity.

The change in the memristor current $I_{mem}$ with applied voltage $V_{mem}$ is plotted in Figure 2.3b, where $V_{mem}$ is a train of write (1.25 V) and read (0.2 V) pulses followed with erase (−1.25 V) and read (0.2 V) pulses followed again with random voltage write/erase and read pulses starting at 2.5 s. The positive voltage pulses increase $I_{mem}$ due to decreases in memristance. On the other hand, the negative voltage pulses lead to a decrease in the current flowing through the device, due to an increase in the memristance. The random pulses show similar behavior in proportion. Similar experimental results are reported in [99].

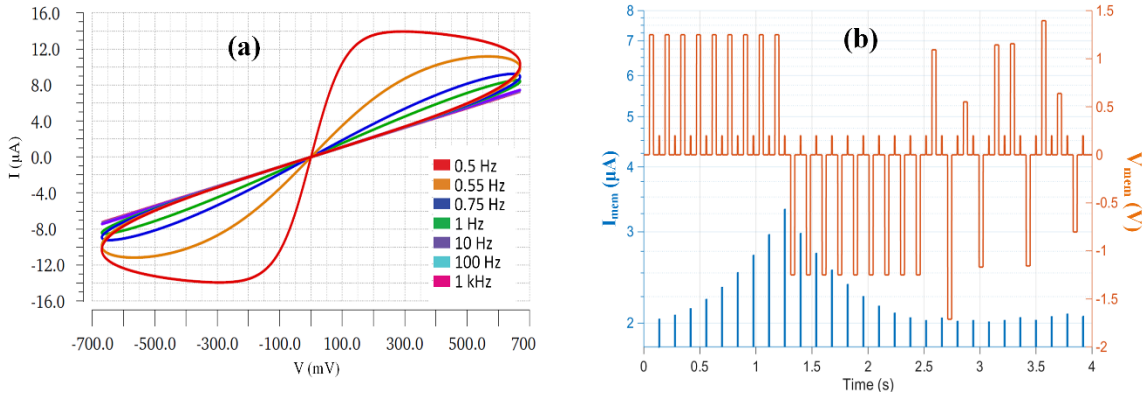


**Figure 2.3.** (a) I-V characteristics of the memristor model used in the study. (b) The current and voltage plot in time shows the increase in $I_{mem}$ as a train of a positive pulse is applied across the device. Similarly, the resistance increases and the current decreases as a train of negative pulses is applied. Only the current measurements during the read cycle are presented here for clarity.

Figure 2.4 shows the electrical characteristics of the memristor behavioral model when the threshold voltage of 0.6 V is included. To analyze the non-linearity in the device, a train of 125 +1 V pulses followed with 125 −1 V pulses are applied with a pulse period of 1 ms and a pulse width of 0.9 ms.

Figure 2.4a and b plot the conductivity and state variable (w/D) of the memristor versus pulse count and device current, respectively. Non-linearity is obvious in Figure a when the device reaches the *off*-state (lowest conductivity) and the slight change in linearity of w/D is also present as the device reaches the *on*-state (highest conductivity). The similar pattern can be observed in Figure b where a logarithmic change in conductance versus current is almost a line, representing a logarithmic change in conductance with device current. Figure c shows the current-voltage characteristic of the device when 0.6 V sine input is applied to the device. Note the I-V curve displays a pinched hysteresis loop and the hysteresis lobe area decreases as input frequency increases, finally reducing to a line at a higher frequency. These are necessary characteristics of the I-V curve of a memristive device [37]. Additional model verification characteristics can be found in [21].

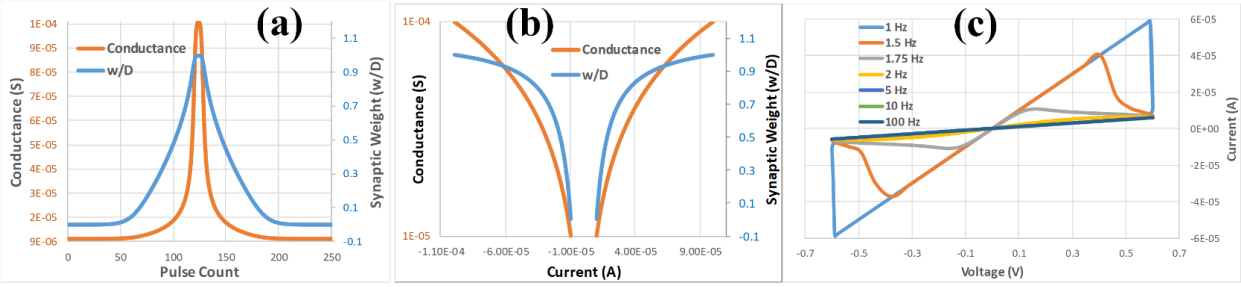


**Figure 2.4.** The memristor device shows a non-linear change in conductance and synaptic weight (w/D) when a train of 125 +1 V pulses followed with 125 −1V are applied (PW=0.9 ms, PP=1 ms). (a) Conductance and w/D versus pulse count and (b) versus device current. (c) The IV curve of the memristor as 0.6 V sine input is applied, showing the characteristic decrease in pinched hysteresis lobe area as frequency increases.

## 2.2 Radiations Effects on Memristors

It is important to model the effects of radiation on the memristive devices to understand the response of systems deployed in harsh environments, such as those experienced during certain military and space missions. Further, nanoscale dimensions of memristors change the way radiation interacts with the devices, often making them more susceptible to single particle events [16]. Multiple studies have experimentally examined the radiation effects on oxide-based memristive devices. Reference [135] discusses the effects of proton and neutron radiation on $TiO_2$ memristive devices. No significant changes in the device characteristics were noticed when exposed to the $3x10^{14}$ 14.1-MeV neutrons/cm$^2$. On the other hand, $7.75x10^{16}$ 350-keV proton/cm$^2$ irradiation is estimated to induce 1.7% additional vacancies in $TiO_2$ leading to an increase in conductivity of the device in the off-state [135]. A similar conclusion is drawn in [143] post proton exposure of their $TiO_2$ memristive devices.

Another experimental study on $TiO_2$ memristive devices in [111] observes the significant change in the on-state of the device post alpha radiation ($10^{14}$ 1-MeV alphas/cm$^2$) although other kinds of irradiation events did not affect the device on-state. Gamma, neutron, and bismuth ion radiation did not affect the off-state of the device, but when exposed to protons and alpha particles the device conductivity increased [111].

The effects of radiation on the electrical characteristics of $TaO_x$ memristive memories are experimentally assessed in reference [144]. Switching from high resistance to low resistance and complete failure of a few devices due to a cumulative dose of 10 keV X-ray irradiation is experimentally observed. Reference [144] also shows that a 220 Co-60 gamma radiation source radiating at a dose rate of 53 rad(Si)/s did not affect the $TaO_x$ device samples. A 4.5 MeV protons source up to a dose of 5 Mrad(Si) did not affect the state of the devices, but when irradiated with protons of energy 105 MeV, the off-state resistance of the devices generally decreased with

increasing proton fluence, indicating cumulative device degradation. Bombardment with 800 keV Si ions created oxygen vacancies in the device, which lead to the loss in resistance similar to the results observed in $TiO_2$ devices in [144].

Proton-based total-dose irradiation effects on Cu-doped-$HfO_2$-based ***resistive-random-access-memory (ReRAM)*** devices are experimentally studied in [145]. Results show positive shifts in the set, reset and on-resistance after proton irradiation, possibly due to induced electron trap changes in $HfO_2$ layer. The effects are observed to enhance almost linearly when the dose increases from 1.5 to 3 to 5 Giga-rad[Si] at a constant dose rate of 237 ± 1.8 krad[Si]/s. Proton irradiation also decreased the off-resistance of the device, by creating more defects and thus increasing the device leakage current [145].

Reference [146] also experimentally investigates the effects of high dose rate ionizing radiation and total ionizing dose on $TaO_x$ memristors. Data shows that the dose rate of $1x10^8$ rad(Si)/s, with a radiation pulse width of 1 μs, did not affect the off-resistance of the device. On the other hand, when exposed to a higher dose rate of $4.3x10^8$ rad(Si)/s for 500 ns, the off-resistance of the devices decreased [146]. In the case of X-ray irradiation (dose rate of $4.3x10^8$ rad(Si)/s), the lack of a discharge path due to the floating terminal setup leads to a decrease in the off-resistance of the device (pointing to circuit setup dependencies) [146]. Reference [146] also uses a $^{60}Co$ proton source to evaluate total ionizing dose-response, the state change was observed at the dose rate of $4x10^8$ rad(Si)/s but not at $1x10^8$ rad(Si)/s. The study indicates that the irradiation response was dependent on the irradiation conditions, bias configuration and varied from device to device [146].

The impact of the proton, gamma and alpha irradiation on the retention and endurance of Ag filament-based ReRAMs (with amorphous $Ge_{30}Se_{70}$ (photo doped with silver) as an active layer) is experimentally studied in [147]. It is noted that devices were able to retain their states until 2.8 Mrad of gamma radiation from $^{60}Co$. The cumulative distribution of on- and off-resistance of the devices following 100 keV electron exposure was one aspect that was carefully studies. *On*-resistance does not seem to vary with irradiation but *off*-resistance decreases as the total ionizing dose becomes higher than 1000 krad. This characteristic was observed in all the cases when the device was programmed at 10 μA, 50 μA and 100 μA pre-exposure [147].

In all the studies mentioned, the devices were able to recover their states after a few cycles and no permanent damage was observed. Studies show that memristors have excellent resistance to damage from certain types of irradiation, but are susceptible to others to a certain extent, and might be a suitable candidates for radiation-hardened electronic networks.

There are multiple ways radiation can affect a memristive device. Device structure, radiation-type, dose, duration, bias, area, and direction appear to play a major role in the response of memristor memory to irradiation. This section groups the observed behavior of the memristors (under radiation) in three different categories: interaction events that only change the state, those that cause ionization, and events that alter the $R_{off}$ (*off*-state resistance) value of a memristor. The radiation model detailed later in this section is motivated by these three observed behaviors.

### *State-Altering Radiation*

Some radiation interaction events will change the conductive state of the device. Such radiation effects have been experimentally observed in most of the oxide-based devices. Proton irradiation in $TiO_2$ [135], alpha irradiation in $TiO_2$ [111], [143], proton irradiation in $TaO_x$ [144], proton irradiation in $HfO_2$ [145] and alpha and proton irradiation in $Ge_{30}Se_{70}$ ReRAMs [147] all showed the decrease in resistance post-radiation when set in the off-state.

***Ionizing Radiation Current***

In some cases (especially interactions with charged particles), atoms in the device will be ionized. This will generate $e^{-}h^{+}$ pairs in the device active region thereby generating current. According to reference [27], gamma rays can cause ionization, though the radiation dose deposited on active layer was only about 31% of total radiation exposed. High energy Bi ions used in reference [27] also shows ionization. However, no change in $R_{on}$ or $R_{off}$ was observed in either of the cases. Similar ionization effect was also experimentally observed in reference [38].

***$R_{Off}$ Resistance Change***

This case models the situation when a radiation event will change the off resistance ($R_{off}$) of the device, thus also changing the read window. This was experimentally observed when the chalcogenide phase change devices were exposed to gamma and electron radiation [39] . Proton radiation was also experimentally observed to decrease $R_{off}$ in Cu filament based ReRAM devices by creating more defects and potentially increasing the device leakage current [40]. Similar changes in $R_{off}$ are also observed in references [32], [38] as a result of silicon ion and alpha irradiation.

***Ionization and State Change Events***

This occurs when an interaction event results in both $e^{-}h^{+}$ pair creation in the device and changing the state of the device simultaneously. These effects due to gamma radiation were experimentally observed specifically in $TiO_x$ based memristors [26], [27], [41].

## 2.3 Memristor SPICE Model With Radiation

This section describes a SPICE model that will capture the behavior of memristive devices in the radiation interaction events described above. In the model, a current source Irad_sc is added to the auxiliary circuit shown in Figure 2.5 that effectively changes the state of the device (stored as the voltage $V_c$ across the capacitor). The current Irad_sc must be added in parallel to $G_x$ such that both currents sum before being multiplied by window function *f*(x). This will still keep state variable w/D bounded within limits of zero and one. Thus, in the radiation model as shown in Figure 2.5, Equation (2.6) becomes:

$$\frac{dV_c}{dt} = (G_x + \text{Irad\_sc})\, f(x), \qquad \begin{matrix} \text{if } 0 < \dfrac{w}{D} < 1, \quad f(x) = 1 \\ \text{else}, \qquad f(x) = 0 \end{matrix} \tag{2.9}$$

On the other hand, a current Irad_eh is added to the main memristive circuit to represent ionizing current (Figure 2.5). It adds to $I_{mem}$ directly without affecting the state variable of the device.

In the overall schematic shown in Figure 2.5, the portion inside the grey box is coded using Verilog-A. This model is essentially agnostic to the type of materials used in the memristor and the exact source of radiation. In the absence of radiation, the model reverts to the standard ideal model.

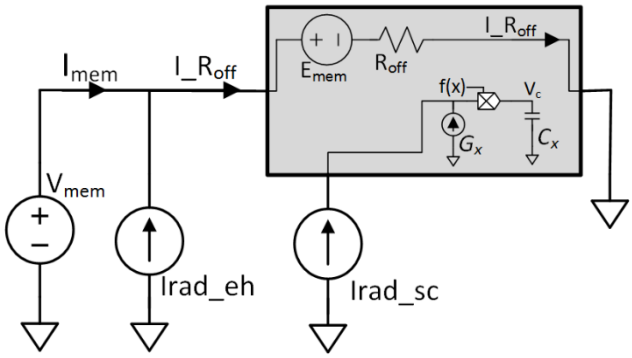


**Figure 2.5**. Memristor model with radiation effects implemented in Cadence Virtuoso. Irad_eh is in parallel with source thus adding to Imem directly without affecting the sate variable. Irad_sc added to the auxiliary circuit so it can modify the state of device instantaneously. Roff is modified as a variable in Verilog-A.

The Spectre transient simulation tool is used in Cadence to generate all the following waveforms. It is important to note that the radiation current values used in the simulation do not necessarily correspond to physical values at this time, but they would be suitable for experimental observations in order to model an actual device. In the following simulations, $I_{mem}$ is the current flowing through the applied voltage source $V_{mem}$, and Cadence assumes the direction of current through an element is towards the closest ground (passive circuit convention). For example, in the case when $E_{mem} > V_{mem}$, $I_{mem}$ measured through $V_{mem}$ by the Cadence simulator will be positive because it follows that as direction of current flow for element $V_{mem}$. In this case, if we follow the current direction assumed in Figure 2.5, the current though the memristor and $V_{mem}$ will be negative with same magnitude. Also, the w/D ratio (state variable) is measured as voltage between 0 and 1 V (1000 mV) in the simulation.

***Radiation-Induced State Change***

Changes in the w/D ratio (difference between initial w/D and final w/D) when IRad_sc is applied, under different device initial conditions are plotted in Figure 2.6. Application of positive IRad_sc increases w/D and thus Δw/D ratio is moves in positive direction. Negative IRad_sc moves the Δw/D ratio in negative direction. In the case when the device is initialized at w/D=0.25, Δw/D is varying from +.75 to −.25 as expected, since w/D is limited from zero to one by window function f(x). Similarly, in case of initial w/D=0.5, Δw/D is varying from +.5 to −.5, and in case of initial w/D=0.75, Δw/D is varying from +.25 to −.75 as expected. The initial values of 0.25, 0.5, and 0.75 were chosen simply for equal spacing between the bounds of w/D. Figure 2.6 also simulates the effect of an IRad_sc pulse width. It is noted (in case of initial w/D=0.25) that higher pulse width (longer duration of radiation IRad_sc) of 1.5 ms, the device reaches its limit at very small IRad_sc of less than 5 mA. On the other hand, at smaller pulse width of .5 ms, higher IRad_sc of more than 15 mA needed to achieve saturation. Other initial conditions display similar pulse width behavior. Thus, we can conclude that the change in the state of the device in affected by both magnitude and duration of the radiation current IRad_sc, and further analysis of these results is ongoing. Δw/D and IRad_sc pulses are varied so as to capture their effect over the wide range. Similar experimental results were reported in references [26], [41]. Δw/D will also be affected by the initial state of the device though most experimental studies present in literature are done on devices in the off-state.

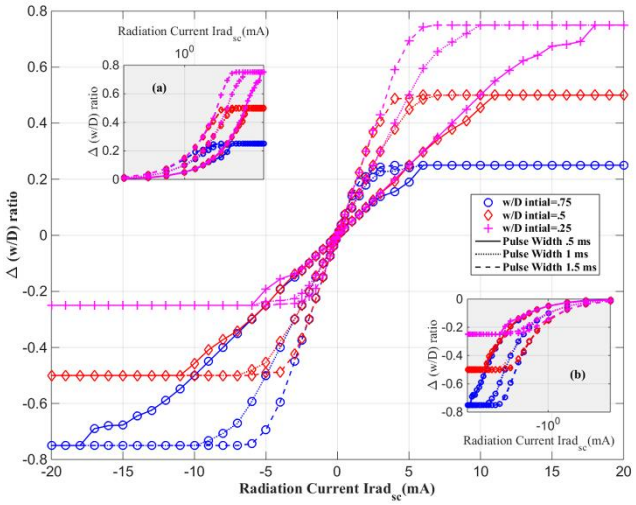


**Figure 2.6.** Change in state (w/D ratio) of device when exposed to IRad_sc of different magnitude and duration. The device is studied under multiple initial conditions evenly spaced between the state variable w/D bounds of zero and one.

Figure 2.7 illustrates the effect of IRad_sc on w/D and $I_{mem}$ in a transient simulation. Figure 2.7a shows the input $V_{mem}$ pulse train of −500 mV with pulse width of 150 ms and Figure 2.7b shows the IRad_sc spiking to 3 mA for 1 ms at 0.8 s, 2.6 s and 4.4 s. In Figure 2.7d, every time IRad_sc occurs, the state of the device switches immediately. At 0.8 s when first IRad_sc pulse appeared, the device was in the off-state, so the state of the device changed immediately but $I_{mem}$ in Figure 2.7e did not increase until the device is turned on again at 0.9 s. Since in this case IRad_eh was not present, according to Figure 2.5, $I_{mem} = I\_R_{off}$ in Figure 2.7f. When the next IRad_sc radiation pulse appears at 2.6 s, the device was in the on-state, so the state (w/D) and $I_{mem}$ change simultaneously. The w/D achieved for IRad_sc pulse at 0.8 s is higher that at 4.4 s because right before 4.4 s device was in much lower w/D state than right before 0.8 s pulse. Thus, the initial state will affect the final magnitude of the state change for same radiation pulse. Additional state changing radiation applied via IRad_sc in itself will not be the source of any current through the device.

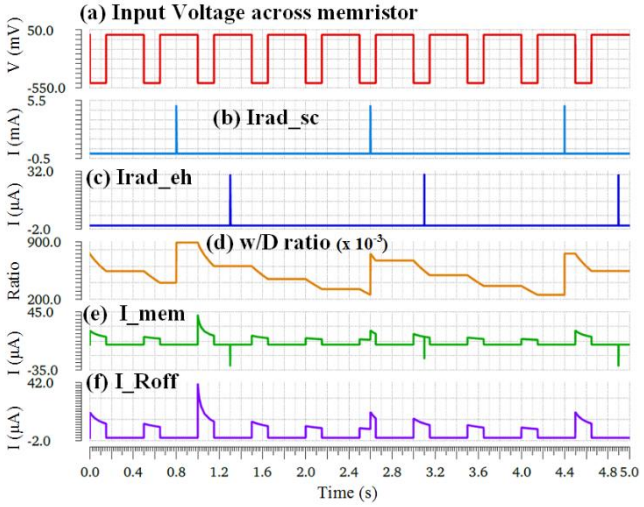


**Figure 2.7.** (a) Input voltage applied ($V_{mem}$) is a train −500 mV pulses with width 150 ms. The effect of radiation that leads to device (b) state change and (c) ionization on (d) w/D ratio. (e) The corresponding $I_{mem}$ and (f) memristor current ($I\_R_{off}$).

IRad_sc shows similar effect in Figure 2.8. An input $V_{mem}$ pulse train with 40 mV pulse magnitudes and pulse widths of 150 ms are applied as shown in Figure 2.8a. The Irad_sc and Irad_eh current pulses are shown in Figure 2.8b and c, respectively. It is interesting in Figure 2.8d that w/D saturates to one very quickly after just two pulses of IRad_sc radiation and high $I_{mem}$ is observed through the device in Figure 2.8e.

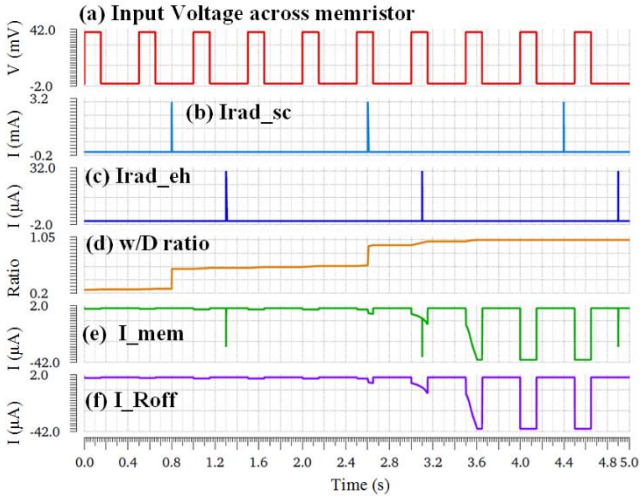


**Figure 2.8.** (a) Input voltage applied ($V_{mem}$) is a pulse train of 40 mV with pulse width of 150 ms. Low negative voltage is chosen to clearly see the changing state overtime. The effect of radiation that leads to device (b) state change and (c) ionization on (d) w/D ratio, (e) $I_{mem}$ and (f) $I\_R_{off}$.

### *Effects of Ionizing Radiation*

The effect of ionizing radiation pulses (captured via IRad_eh) is shown in Figure 2.7c where radiation hits the circuit at 3 mA for 1 ms at 1.3 s, 3.1 s and 4.9 s. Both $I_{mem}$ in Figure 2.7e and $I\_R_{off}$ in Figure 2.7f are not equal when IRad_eh arrives. Active voltage source compensates for increase in IRad_eh thus, $I\_R_{off}$ observes no change due to ionization event i.e. IRad_eh does not affect the state or the current passing through the device.

IRad_eh shows similar effect in Figure 2.8 where input Vmem pulse train is positive in Figure 2.8a. Even after w/D saturates in Figure 2.8d, IRad_eh radiations does not affect $I\_R_{off}$ device in Figure 2.8f. Similar results are experimentally recorded in [26] where no detectable effect of ionization is observed. On the other hand, the experimental results in [38] indicate no changes in memristive devices at lower x-ray radiation dose but higher dose rate changed the off resistance of device which might be due to changes in physical structure.

### *Changes in Off-State Resistance*

Alpha radiation experimentally leads to state change in $TiO_2$ devices in [27], but no change in $R_{off}$ or $R_{on}$ are reported in their devices contrary to alpha radiation studies done on $TiO_2$ devices in [42], which shows change in $R_{off}$ due to device deterioration. Our model considers that radiation may lead to changes in both $R_{off}$ and the state of the device, as depicted in Figure 2.9. Input ($V_{mem}$) in Figure 2.9a is a pulse train of −500 mV pulse magnitude and pulse width of 150 ms, is chosen so as to observe the effect of change of resistance more clearly. In Figure 2.9b, IRad_sc enters the device after 2.4 s producing 5.6 mA of current for 1 ms (device is in off state at 2.4 s). This instantaneously lowers the off-resistance of the device from 100 kΩ to 50 kΩ as in Figure 2.9e. In Figure 2.9c, initial w/D=0.75 at 0 s and as Irad_sc hits the device at 2.4 sec w/D instantaneously switches back to initial value of 0.75 (Irad_sc was chosen as such). Further, even though the w/D value is the same at 0 s and

2.5 s, the current $I_{mem}$ is almost twice as much at 2.5 s (Figure 2.9d) because the $R_{off}$ decreases (to half from 100 kΩ to 50 kΩ) as result of radiation. Thus, the device is letting through higher current even in the more resistive state. In addition, Figure 2.9d demonstrates that the Δw/D has changed considerably due to radiation event, going from 0.56=0.75−0.19) pre-radiation to 0.744=0.75−0.006 post-radiation for identical input pulses applied. This indicates that the read window has decreased for the device post radiation. At the moment, we do not apply changes to $R_{off}$ due to Irad_eh. Similar results can be observed in experimental studies performed in references [38]–[40], [42].

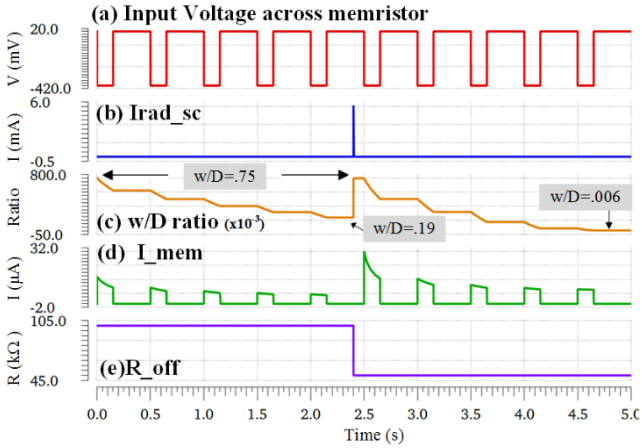


**Figure 2.9.** (a) Input voltage applied ($V_{mem}$) is a pulse train of −500 mV with pulse width of 150 ms. Voltage is chosen as such to clearly see the effect of changing $R_{off}$ on device. (b) The radiation pulse (IRas_sc) that would change the off resistance of the device (c) shows the increase in w/D ratio and, (d) $I_{mem}$ as radiation hits the device. (e) Shows the decrease in $R_{off}$ post radiation event.

### *Stochastic Radiation Effects*

Characteristically radioactive decay magnitude follows random Gaussian distribution and the pulse interval follows the random Poisson distribution [149], [150]. Figure 2.10 presents the radiation current spikes following Gaussian and Poisson distribution such that the memristive device will see the radiation current spikes at 5.6123 Hz average frequency.

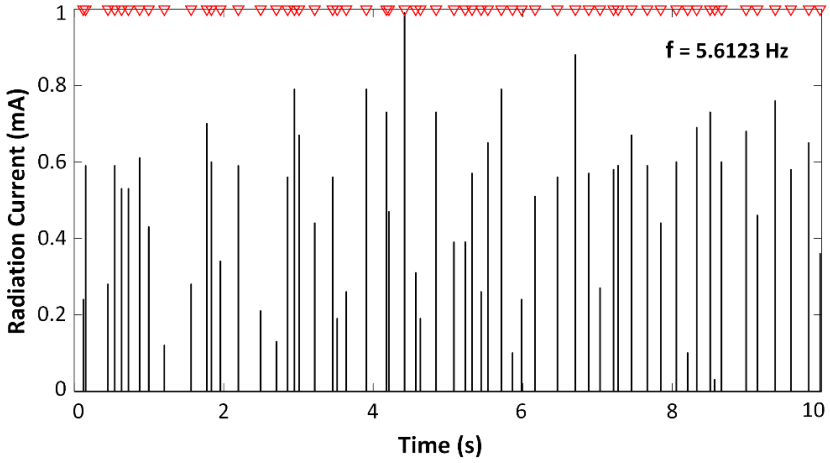


**Figure 2.10.** The sample distribution of the radiation current spikes for 10 s at an average frequency of 5.6123 Hz. Current pulse magnitude follows the random Gaussian distribution and the pulse interval follows the random Poisson distribution.

Figure 2.11a plots the histogram showing the ***inter-spike interval (ISI)*** between consecutive spikes from Figure 2.10. The histogram shows the desired Poisson distribution with λ = 0.25 s. The histogram in Figure 2.11b plots the current magnitude distribution of each radiation current pulse. The histogram shows the Gaussian distribution of the magnitude. In this case, the mean and standard deviation of the current magnitude is 0.5 mA and 0.25 mA respectively. Throughout this work, radiation frequency is kept at an average of 5 Hz with a standard deviation of 1 Hz, although mean and standard deviation are modified to simulate the desired intensity.

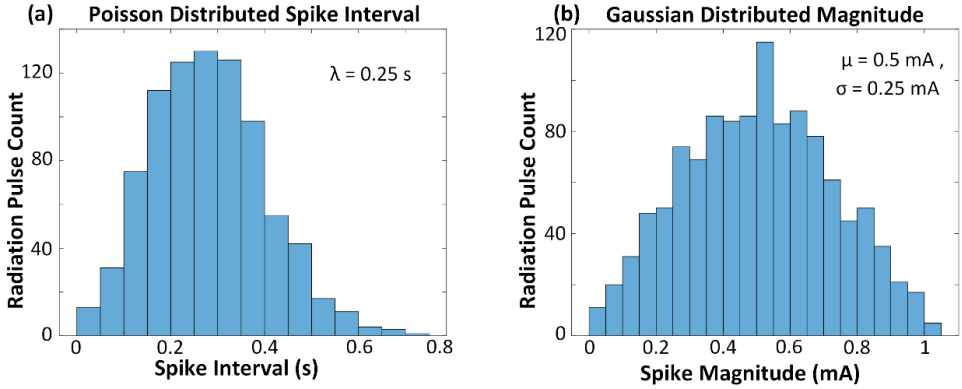


**Figure 2.11.** Histograms show the radiation current (a) spike interval distribution and (b) spike magnitude distribution. The pulse magnitude follows random Gaussian distribution and the pulse interval follows the random Poisson distribution.

In Figure 2.12, the effects of $Irad_{sc}$ and $Irad_{eh}$ are simulated when they are occurring simultaneously due to radiation, but do not change the off-resistance of the device. The input ($V_{mem}$) in Figure 2.12a is a train of −650 mV pulses with width 150 ms is applied directly to the device. The Irad_sc in Figure 2.12b and Irad_eh in Figure 2.12c are generated such that the current magnitude follows random Gaussian distribution and the pulse interval follows the random Poisson distribution.

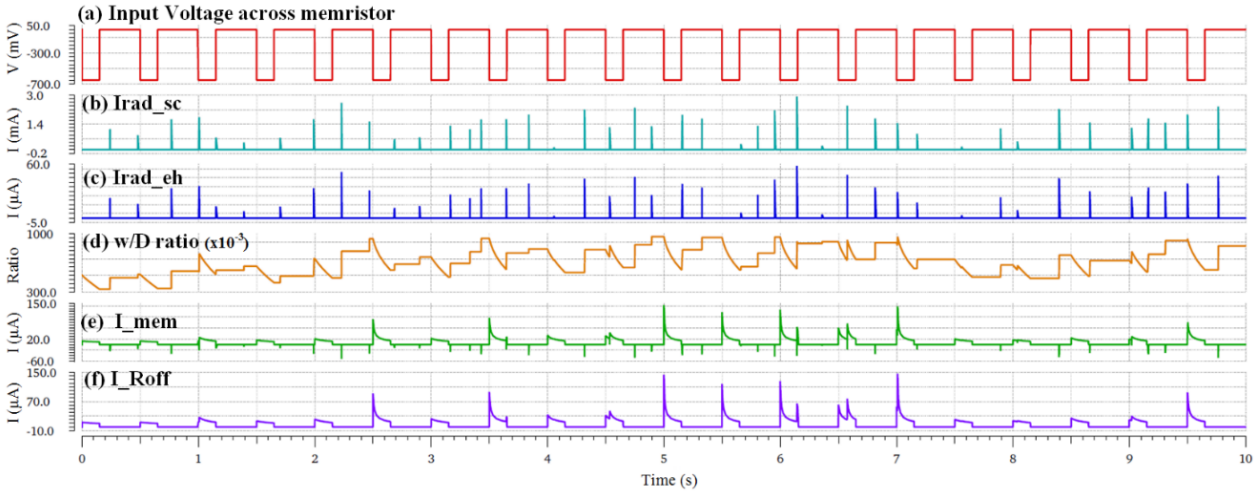


**Figure 2.12.** (a) Input $V_{mem}$ applied at −650 mV amplitude and 150 ms pulse width. (b) Irad_sc, state change radiation and (c) Irad_eh, ionization radiations. Both $Irad_{sc}$ and $Irad_{eh}$ are generated randomly, with Gaussian distributed magnitude and Poisson's distributed interval (d) $\frac{w}{D}$ ratio changes accordingly and reached to the maximum often but stays in the limit. (e) $I_{mem}$ balances Irad_eh and (f) Irad_sc modifies the state of the device and $I_{Roff}$ in proportion to its magnitude and state of the device right before the event.

The result obtained follow the behavior observed in Figures 2.7 and 2.8. $I_{mem}$ balances Irad_eh during each event, so device current or state are not affected. On the other hand, Irad_sc modifies the state of the device in proportion to its magnitude and the state of the device right before the event. Similar results can be observed in [111], [134], [144]. $\frac{w}{D}$ reached a maximum value of one at multiple places such as at 2.5 s, 4.9 s, and around 6 s but always stays bound within the limits of $0 < \frac{w}{D} < 1$.

## 2.4 Spiking Neuron Circuits

The post-synaptic neuron used in the biphasic spiking neural network is designed in Verilog-A with code provided in Appendix B. It represents a ***leaky integrate-and-fire (LIF)*** circuit behavior governed by the Hodgkin-Huxley equations. The LIF circuit is implemented in the literature using a single operational amplifier and MOSFETS [151]–[153]. This behavioral model increases the speed and efficiency of the simulated circuit relative to one with actual components. The LIF circuit fires a bidirectional biphasic spike toward the dendritic and axonic synapses when a certain threshold is reached. A schematic depiction of the LIF circuit is presented in Figure 2.13a. The input of the circuit, $V_{PostIn}$, is the node connected to the output of all the post-synaptic memristors in a network. $V_{PostIn}$ changes with the change in the conductivity of the memristors and the spike timing of the pre-synaptic afferents in the neural network.

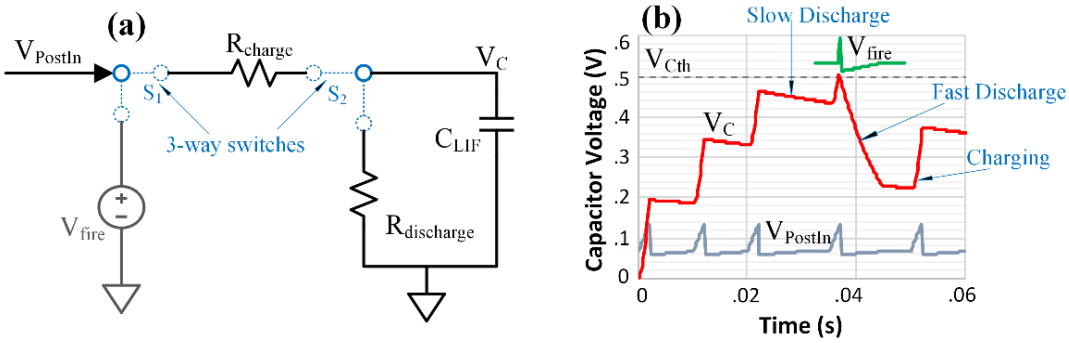


**Figure 2.13.** (a) Leaky integrate-and-fire (LIF) post-synaptic neuron circuit. The circuit is designed in Verilog-A. The voltage source $V_{fire}$ produces the desired shape of post-synaptic biphasic spike. $C_{LIF}$, $R_{charge}$, and $R_{discharge}$ are responsible to mimic the leakiness of the biological synapse. (b) The plot shows the increase in the voltage across capacitor $C_{LIF}$ as the circuit sees the input spikes over time ($V_{PostIn}$). $V_{fire}$ sends out the output spike as $V_C$ reaches threshold voltage $V_{Cth}$ (= 0.5 V in this case).

In Figure 2.13a, the switches $S_1$ and $S_2$ are initially connected to $R_{charge}$ (1 GΩ), thus charging $C_{LIF}$. If, at any point, $V_{PostIn}$ is less than the voltage across $C_{LIF}$, $S_2$ flips and $C_{LIF}$ starts discharging via $R_{discharge}$ at 20 GΩ for a slow leak. As soon as $V_{PostIn}$ is larger than the voltage across $C_{LIF}$, $S_2$ flips back and $C_{LIF}$ starts charging again via $R_{charge}$ at 1 GΩ. At times when the voltage across $C_{LIF}$ becomes greater than a certain threshold, $S_2$ connects to $R_{discharge}$ and $S_2$ connects to $V_{fire}$ and the circuit fires a desired biphasic spike, designed in the Verilog-A code. In this condition, $R_{discharge}$ is at 1 GΩ for quick $C_{LIF}$ discharge or reset, and $V_{fire}$ produces a biphasic spike traveling toward the memristors (axonic synapses), thus updating their weight via the STDP learning rule. The charging and discharging states of the capacitor are shown in Figure 2.13b using the red trace. As the input spike arrives the capacitor charges and discharges slowly in the absence of a positive spike. The charging and discharging process continues until just before 40 ms in Figure 2.13b, when the capacitor reaches a threshold ($V_{Cth}$ = 0.5 V in this case). At this point, $V_{fire}$ fires a bidirectional biphasic spike, which is sent towards the present and the next layer of memristors (dendritic synapse) in the network (not used in this work). The capacitor discharges rapidly during the time $V_{fire}$ is firing the biphasic spike, as shown in Figure 2.13b as the green trace.

The threshold ($V_{Cth}$) for the voltage across $C_{LIF}$ in Figure 2.13a, which would lead to the post-synaptic afferent fire, depends on various factors. These factors include and are not limited to the number of afferents used in the network, the charging, and discharging time constants, the pre-synaptic pulse width, the frequency, and the amplitude. Too low of a threshold may make the network unstable by changing the weights too fast. On the other hand at too high of a threshold, the network weights may not change much or at all and thus the network would be unable to learn.

# 3. Neural Network Design

The network simulations in this work are generally of two topologies, as shown in Figures 3.1 and 3.2. Both memristor-based neural networks are fully connected, where all the pre-synaptic afferents are connected to all the post-synaptic afferents via single memristors. The networks are also unsupervised and are feed-forward, i.e. the connections between the nodes are not cyclic, unlike recurrent neural networks. The conductivity of the memristors is modified continuously depending on the activities of the two connected neurons.

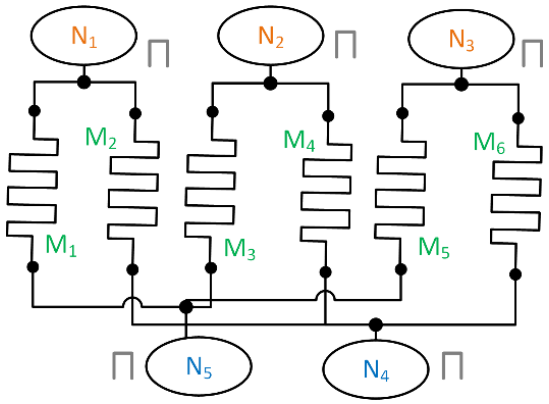


**Figure 3.1.** The memristor-based electronic pulsed neural network. Three pre-synaptic neurons are each connected to two post-synaptic neurons via memristors used as synapses. This network uses randomly occurring digital square pulses to modify the synaptic weights.

The pulsed neural network shown in Figure 3.1 has all three pre-synaptic neurons ($N_1$, $N_2$, and $N_3$) electrically connected to two post-synaptic neurons ($N_4$ and $N_5$) via six memristors ($M_1$ to $M_6$). This network uses square digital pulses as the action potentials and is used for preliminary simulations. The second topology is represented by a spiking neural network in Figure 3.2, and is a single layer perceptron network with either 25 or 100 pre-synaptic afferents ($N_1$ to $N_{25/100}$), each connected to a single post-synaptic neuron (LIF post N) via single memristors ($M_1$ to $M_{25/100}$). This network is used to learn the desired 25-pixel or 100-pixel pattern via the STDP learning rule.

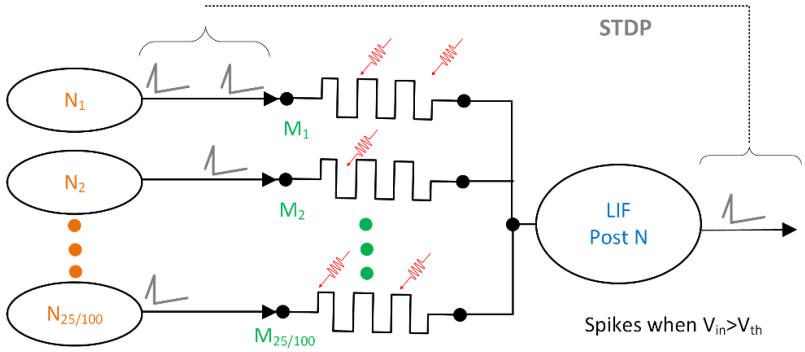


**Figure 3.2.** The memristor-based electronic Spiking Neural Network used in this work for spatio-temporal pattern recognition (STPR). 25 or 100 pre-synaptic neurons are connected to one post-synaptic leaky integrate-and-fire (LIF) neuron via single memristors. The network uses biphasic shaped pulses to achieve pair-based STDP for pattern learning.

## 3.1 Pair-Based STDP

As mentioned previously, STDP is a biological process that changes the strength of the connection between two neurons based on pre- and post-synaptic neuron firing time. Many variations of STDP

are observed in biological in different areas of the brain and across different species. The STDP rule implemented in this research is closest to one observed in the neocortex layer of the hippocampus region in the human brain [154], [155]. In memristive devices, different shapes of pre- and post-synaptic neuron spikes can be used to obtain the desired STDP shape [156]–[159] Often, a simple pair-based STDP implementation is used, although frequency-dependent effects are typically observed in neuroscience experiments, as in [160]. This section discusses the effects of various factors on the STDP learning curve.

Figure 3.3 shows the test structure used to capture the STDP relationship. The memristor is connected to a source of pre-synaptic and post-synaptic biphasic spikes entering into the two terminals. The pre- and post-synaptic 10 ms biphasic spikes arrive at different time intervals as in Figure 3.3a and b. Due to the time difference in the shaped pulses, the memristor sees varying potential across it as shown in Figure 3.3c. When this net potential reaches sufficient magnitude (which depends on the memristor threshold), a spike pair can change the synaptic weight.

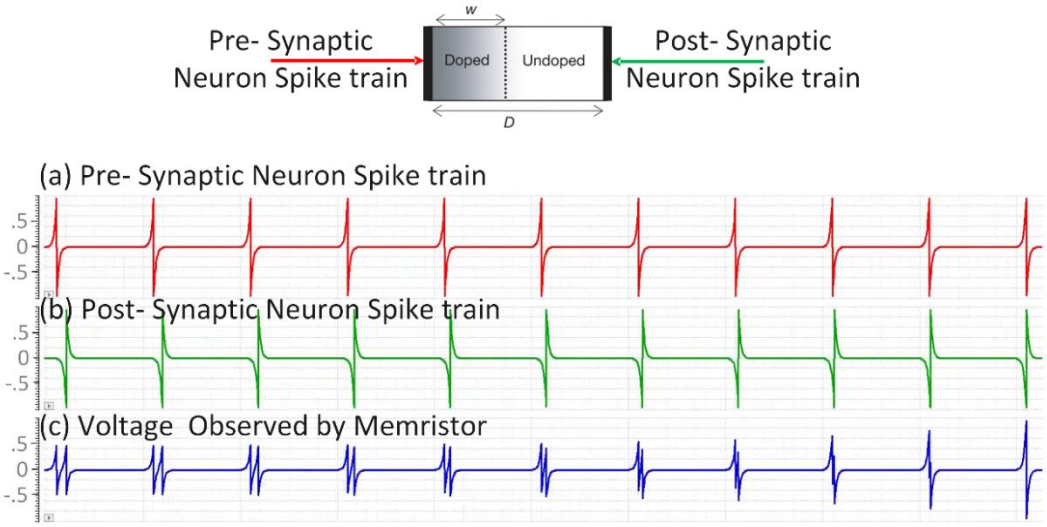


**Figure 3.3.** The two terminals of a Memristor are connected to the pre- and post-synaptic neuron inputs. Spike trains in (a) show the pre-synaptic neuron spike produced and (b) shows the post-synaptic neuron spike observed by the memristor terminal. The magnitude and shape of both are the same, except there is a difference in their arrival times. Due to the difference in arrival time, memristor observes the voltage given in (c) across it. Thus, the synaptic weight change would be different at each pre-post pairs' arrival, resulting in the STDP curve.

***Dependence on State Variable and Pulse Shape***

The pair-based STDP curve in Figure 3.4a is obtained using exponential biphasic spikes, whereas the results in Figure 3.4b are generated using triangular biphasic spikes, as shown in the respective insets. In Figure 3.4, the magnitude of change in synaptic weight ($\Delta\frac{w}{D}$) at any given time will depend on the initial synaptic state of the device and on the shape of the pre- and post-synaptic pulses.

When the device was initially in a less conductive state of $\frac{w}{D} = 0.1$, it saw about a six to ten times larger change in synaptic weight when compared to when the device was initially at 90% $\frac{w}{D}$, i.e. in a highly conductive state. This was due to the non-linearity present in the device. Also, the difference in the shape of the STDP curve for different action potential shapes can be observed in the figure.

The triangular spikes in Figure 3.4b gives more distinct and sharper changes in the $\Delta\frac{w}{D}$, while the exponential input in Figure 3.4a provides a gradual larger change in the $\Delta\frac{w}{D}$ with up to 6%, as compared to 2% due to the triangular spikes. This is due to non-linearity in the potentiation of the exponential curve.

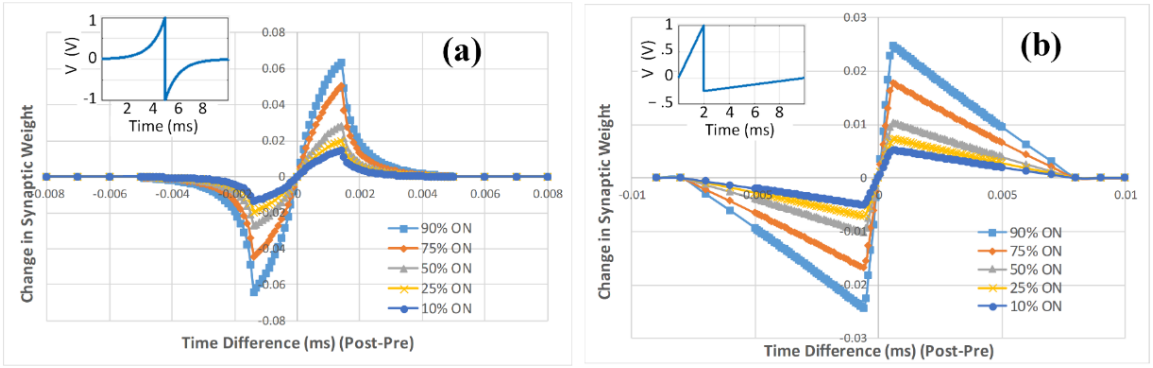


**Figure 3.4.** Different STDP shapes obtained using (a) exponential and (b) triangular biphasic pulses as seen in the respective insets. The magnitude of change in synaptic weight ($\Delta\frac{w}{D}$) also increases if the device was initially in the lower conductive state that is due to the non-linearity of the memristor model.

***STDP Dependence on Memristor Threshold***

The STDP curves in Figure 3.5 areFigure collected using exponential biphasic spikes, as shown in the inset. In this case, the threshold $V_{th}$, of the synaptic memristor device is changed from 0.25 V to 1 V, observing the change in STDP. In the case when the threshold is set to 0.5 V, the memristor will not change its state until the voltage drop across it is equal to or greater than 0.5 V (the threshold).

As the magnitude of $V_{th}$ decreases in Figure 3.5, the read window increases for the same 100 ms pulse. The read window is the duration where a memristive device will see the change in the weight ($\Delta\frac{w}{D} > 0$) due to the arrival of pre- and post- synaptic spike. In the case of $V_{th}$ equal to the 0.5 V, the learning window is 120 ms because $\Delta\frac{w}{D}$ is not zero for $-60$ ms $< \Delta t >$ 60 ms. On the other hand, in the case of $V_{th}$ equal to the 1 V learning window is only 70 ms because $\Delta\frac{w}{D}$ is not zero for $-35$ ms $< \Delta t >$ 35 ms. Lower threshold ($V_{th}$) values result in a larger read window and the magnitude of the $\Delta\frac{w}{D}$ is severely affected. In Figure 3.5 at $\Delta t$ = 10 ms, if the device $V_{th}$ is set at 0.25 V it observes 50% less change in $\frac{w}{D}$ ($\Delta\frac{w}{D}$ = 1%) as compared to when device $V_{th}$ is set at 0.75 V ($\Delta\frac{w}{D}$ = 2%). At 0.25 $V_{th}$, the network will be unable to distinguish between the pre- and post-synaptic pair arriving between 5 ms and 40 ms ($-5$ ms and $-40$ ms). Thus, the network would be unable to adjust the synaptic weights appropriately and will not learn any certain pattern.

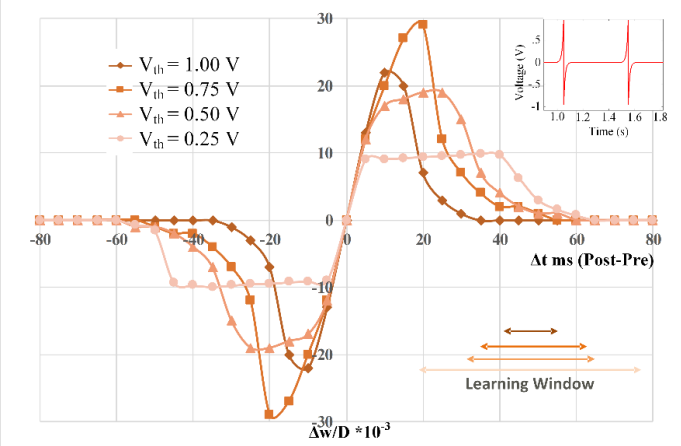


**Figure 3.5.** Change in the STDP learning rule as the threshold of the memristor changes. Input spikes, in this case, are 100 ms, 1V exponential biphasic pulses, as shown in the inset. As the threshold decreases, the learning window increases, but the magnitude of change in the synaptic weight ($\Delta\frac{w}{D}$) decreases and becomes undesirably flat.

### *Effect of Pulse Width on STDP*

The STDP curve in Figure 3.6Figure is collected using exponential and triangular biphasic spikes, as shown in the inset. In this case, the width of the triangular and the exponential spikes is changed to observe the change in STDP. Similar to Figure 3.4, Figure 3.6 also shows that the change in the synaptic weight ($\Delta\frac{w}{D}$) is higher in the case of the exponential spikes when compared to their triangular counterparts. Figure 3.6 also shows that as the pulse width decreases, the read window decreases. The read window for 50 ms pulse width spikes is about 60 ms, and the read window for 100 ms pulse width spikes is about 120 ms. The read window is independent of the pulse shape. The decrease in the read window with pulse width is simply due to the reason that the duration of the spike is small. If the 50 ms pre-synaptic spike will arrive 60 ms before or after the 50 ms post-synaptic spike, they will be too far apart to add up to pass the desired threshold to make any change in the STDP (as depicted by earlier spikes in Figure 3.3).

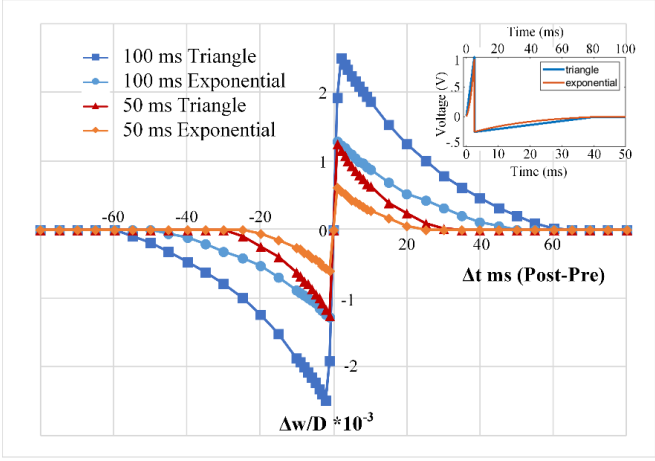


**Figure 3.6.** Changes in the STDP learning rule as the shape and width of the input biphasic spike changes. Input spikes, in this case, are either a triangular or an exponential biphasic pulse of 50 ms or 100 ms, as shown in the inset. As the pulse width decreases, the learning window decreases. It is also observed that the magnitude of change in synaptic weight ($\Delta\frac{w}{D}$) decreases with a decrease in pulse width and pulse shape.

### 3.2 Pattern Learning

The spike encoding scheme used in this work is one in which binary values are translated into regular firing patterns versus random firing. Pre-synaptic afferents ($N_1$ to $N_{25/100}$), in the biphasic spiking neural network in Figure , are typically firing at an average rate of 5 Hz for the 100 s transient simulation time. Afferents that are part of the pattern (a 10-pixel 'B'), as shown by the lighter colors in Figure 3.7b produce mutually correlated spikes at regular interval, as shown in Figure 3.7a, $N_{12}$ and $N_{13}$ [161], [162]. Conversely, non-participating afferents in Figure 3.7b (dark color), fire uncorrelated spikes with Poisson distributed intervals as shown by $N_{14}$ and $N_{15}$ in Figure 3.7a. This same firing pattern is used in generating a 100-pixel 'B' pattern in the larger 100 afferent networks as well.

Pre- and post-synaptic afferents fire a biphasic triangular spike for 10 ms, which potentiates to a peak voltage of +1 V and the depression tail reaches a maximum of −0.25 V, as shown in the inset of Figure 3.6. All of the memristors in the spiking neural networks are initially kept in a conductive state with a resistance distribution varying from 20 kΩ and 35 kΩ, as can be noted in Figure 3.7b (Initial State).

Figure 3.7b shows the synaptic weight evolution of all the memristors ($M_1$ to $M_{25}$) as the network learns the 25-pixel letter 'B' with this training approach. Starting around 30 s, the network was able to depress most of the uncorrelated neurons by decreasing the conductivity of their corresponding memristors and the desired pattern is very recognizable. At 60 s, the network is in a stable state with post-synaptic neurons firing at a constant rate, as the un-correlated neurons are completely depressed and thus not contributing any current to the LIF circuit of the post-synaptic neuron. Figure 3.7c shows the synaptic weight distribution of the memristor and a decrease in the weight of the uncorrelated synapses can be noted at 30 s.

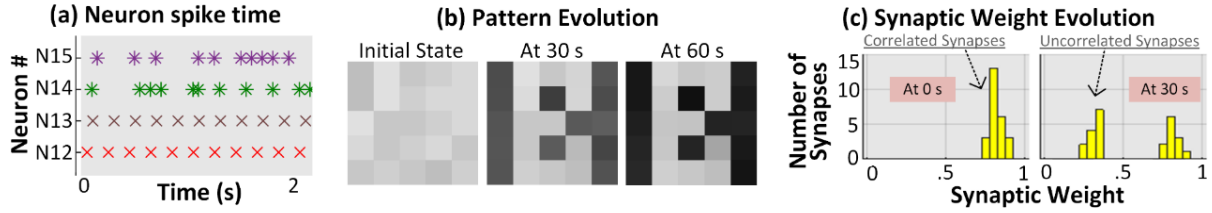


**Figure 3.7.** (a) Scatter plot of the spike times of two correlated afferents N12 and N13 (participating in the pattern) and two non-participating, uncorrelated afferents (N14 and N15). (b) The initial synaptic weight distribution and evolution of the pattern over time as the system is in the process of learning a 25-pixel letter 'B'. (c) A histogram of the synaptic weight distributions in weight bins that are 0.05 wide. After 30 s, uncorrelated neurons are separated and moved to a lower weight.

The STDP data in Figure 3.8 shows changes in the synaptic weights of all 25 memristors for 100 s as a function of the time difference between post- and pre-synaptic spike firing. When a post-synaptic neuron fires after a pre-synaptic neuron (time difference > 0 ms), the network considers them correlated and the synaptic weight of the respective memristor increases, making the synaptic connection more conductive (and vice-versa). The STDP curve shows much stronger depression than potentiation, meaning the network can depress the uncorrelated afferents faster. Asymmetrical STDP curves are obtained using different potentiation for pre- and post-synaptic spikes, as shown in the inset in Figure 3.8.

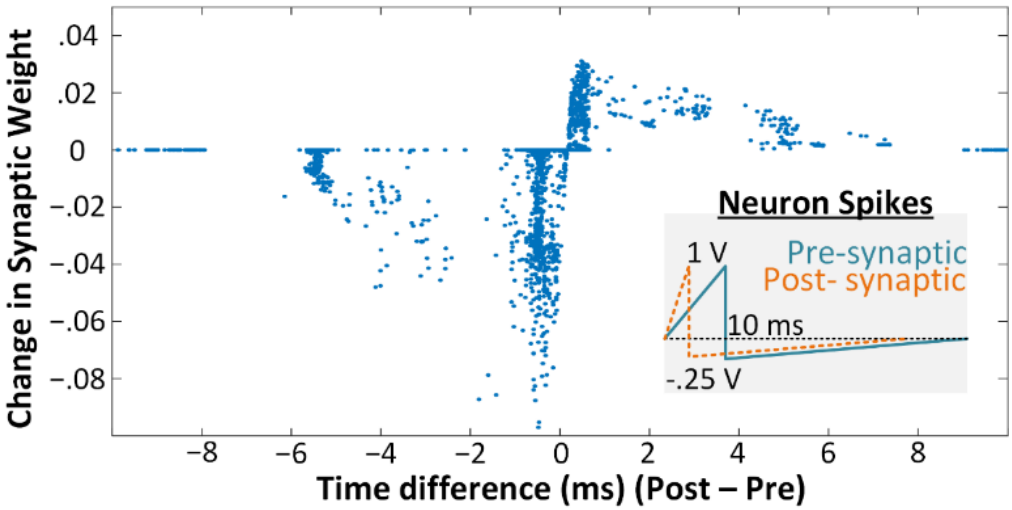


**Figure 3.8.** STDP plot obtained from weight changes due to nearest-neighbor pairs in the 100 s simulation of the network with 25 pre-synaptic biphasic spiking neurons of Figure . Inset shows the pre- and post-synaptic neuron inputs used. STDP has much stronger depression than potentiation, generally leading to faster learning in the network.

# 4. Neural Networks with Radiation

In this section, memristor-based spiking neural networks are used to analyze the effect of radiation on the spatio-temporal pattern recognition (STPR) capability of the networks. The radiation effects discussed in Chapter 3 are simulated on the SNNs and corresponding learning rules presented in Chapter 4. The modified non-linear memristor drift model used is discussed in Chapter 2. All the simulations are captured in Cadence Virtuoso Spectre.

Networks with 5, 25, and 50 neurons are simulated to observe the effect of radiation at different intensities, flux, and periods. The chapter starts by discussing the effects of state-altering radiation on the STDP curve, thus observing the effects of radiation on the expected learning rule. The long-term cumulative effects of radiation current pulses are also observed in the pulsed neural network in the absence of any pattern. Later sections of the chapter discuss the effects of radiation on the spatio-temporal pattern learning ability of the network. Changes in network learning capability and system stability are statistically analyzed as well. The contributions from this chapters are published in [113]–[115].

## 4.1 Radiation Effect on STDP

Figure shows the change in the STDP learning curve as the memristive device is exposed to an event of state-altering radiation before the pre- and post-synaptic biphasic pulses arrive (as indicated in Figure 3.3). Figure 4.1a shows the STDP curve resulting from the exponential biphasic spike and Figure 4.1b results from a triangular biphasic spike, as shown in their respective insets. Radiation is observed to shift the whole curve upward, making it asymmetric. Thus, the system will undesirably favor a stronger correlation and might make the system unstable. The STDP curve is noted at the varying intensities of the state-altering radiation current, the curve shifts more as the radiation intensity increases, indicating that the neural network will be overwhelmed at a higher magnitude of radiation current.

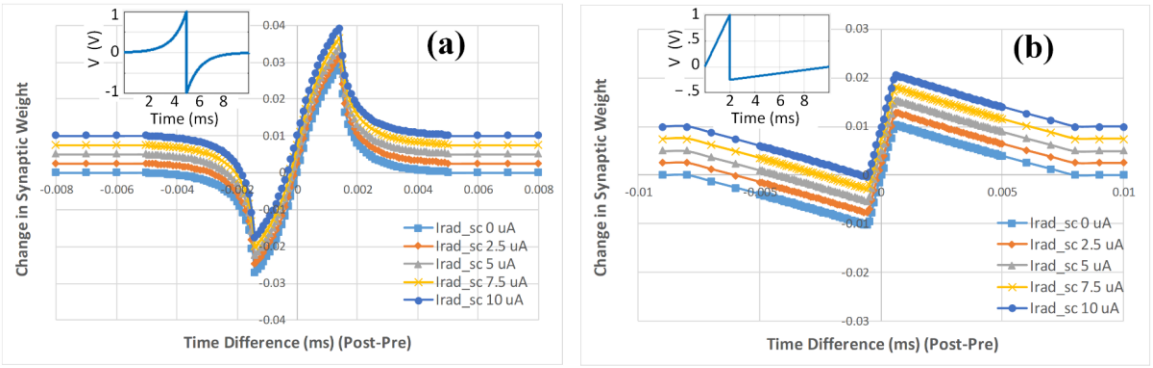


**Figure 4.1.** STDP plot after a state-altering radiation event for (a) exponential and (b) triangular biphasic pulses. The STDP curve shifts upward due to radiation that brings asymmetry into the STDP curve and thus tends to favor an increase in synaptic weight.

## 4.2 Radiation Effects on a Pulsed Neural Network Without Patterns

This section discusses the effects of state-altering radiation current on an SNN which is not in the process of learning any pattern. In this case, the pre-and post-synaptic neurons are not firing any specific pattern, the rectangular pulses (not shaped) simply present randomly distributed Poisson noise.

The network shown in Figure 3.1 is used to study the effect of radiation events on this pulsed neural network. In Figure 3.1, $N_1$, $N_2$, and $N_3$ are pre-synaptic neurons (afferents) and $N_4$ and $N_5$ represent

post-synaptic (output) afferents. Memristors ($M_1$ to $M_6$) in the network represent the synapses electrically connecting neurons. For simulation purposes, five independent voltage sources mimic the behavior of the neurons. Each voltage source generates 500 mV pulses such that the pulse interval follows the random Poisson distribution as shown in Figure 4.2a. Due to the presence of these pre- and post-synaptic voltage pulses, the state or weight ($\frac{w}{D}$) of all six memristive devices will changes interdependently, as shown in Figure 4.2b.

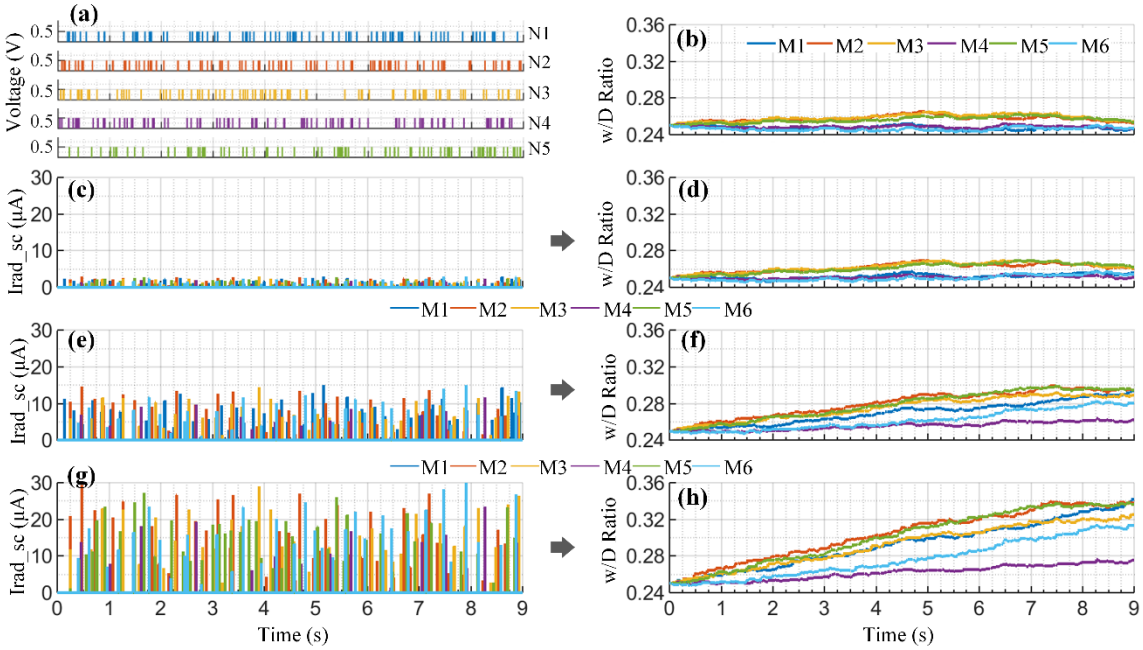


**Figure 4.2.** Simulation of the network in Figure 3.1. (a) Randomly Poisson distributed voltage pulses depicting the behavior of randomly spiking neurons. (b) Synaptic weight evolution with no radiation. The network is exposed to randomly Poisson (interval) and Gaussian (amplitude) distributed radiation events, and then the synaptic weight of each memristor is observed. (c) Low radiation, μ = 1.5 μA, and σ = 0.75μA. (d) Low radiation increased the weights, making the device more resistive. (e) Medium radiation, μ = 7.5 μA, and σ = 3.75μA. (f) Medium radiation increases the weights further and (g) higher radiation, μ = 15 μA, and σ = 7.5 μA, (h) at higher radiation the neuromorphic effect is almost negligible and the radiation events drive the weights considerably, making the device more conductive.

Each synaptic memristive device is exposed to a different state-altering radiation pattern. The radiation current $Irad_{sc}$ pulse interval follows the random Poisson's distribution and the magnitude follows the random Gaussian distribution with mean μ and standard deviation σ. Figure 4.2c, e, and g represent the radiation pattern used on the memristors, which are at different intensities. These radiation events follow the same timing, but their mean magnitude is 1.5 μA, 7.5 μA, and 15 μA and the standard deviation is 0.75 μA, 3.75 μA and 7.5 μA for Figure 4.2c, e, and g, respectively. Plots in Figure 4.2d, f, and h respectively represent the resulting weights of the memristor during the three periods of radiation exposure.

It is noted that at the stronger radiation flux, the synaptic weights deviate farther away from their desired pattern, making synapses more and more conductive. In Figure 4.2g, stronger radiation almost overtakes the effect of the input from the neurons, contrary to the Figure 4.2d effect which saw much less intense radiation flux, and thus still follows the input of the neuron with much less deviation. For an expected memristor device size of 100 nm x 100 nm, the radiation flux in this

example is 4.685 x $10^{10}$ $cm^{-2}$ $s^{-1}$. This is a large value, but certainly one that is observable in many different situations.

Figure 4.3 represents the simulation results obtained using the same fully connected pulsed neural network shown in Figure 3.1. Each afferent in the network generates a train of 500 mV (1 ms) square pulses at Poisson distributed inter-spike intervals representing pure noise (no patterns or correlations). The system is also irradiated for the first 10 s with state-altering radiation of different magnitude (μ = 1 μA to 100 μA, and σ = 0.5 μA to 50 μA) and flux (up to 5x$10^{10}$ $cm^{-2}s^{-1}$). Figure 4.3 plots the $\frac{w}{D}$ of each memristor ($M_1$ to $M_6$) after 50 s of simulation. Although the system is irradiated only for the first 10 s, the radiation effects accumulate over time, and at higher radiation intensity, the weights have considerably diverted. Some will even saturate, as is the case of $M_4$, $M_5$, and $M_6$ at the higher flux of 5x$10^{10}$ $cm^{-2}s^{-1}$. This cumulating behavior of the effect of radiation could lead to pattern learning and recognition challenges in neural networks [113].

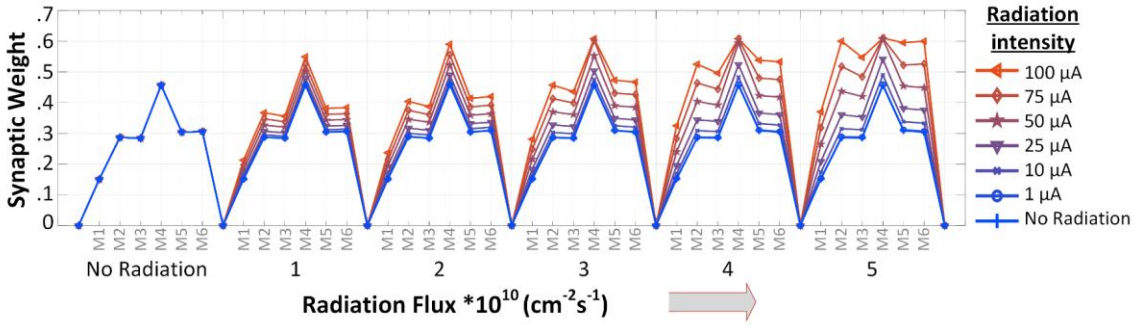


**Figure 4.3.** The synaptic weight ($\frac{w}{D}$) of memristor ($M_1$ to $M_5$) of the fully connected pulsed neural network represented in Figure. The network is simulated using 0.5 V, 1ms square pulses, radiated for 10 s with state-altering radiation of different mean magnitude and flux and the $\frac{w}{D}$ values are noted after 50 s of simulation. The radiation effects seem to cumulate over time, especially from stronger radiation events.

## 4.3 Radiation Effects on Pattern Learning and Recognition

This section discusses the effects of state-altering radiation current on an SNN in the process of learning a pattern. In this case, few of the pre-synaptic neurons that are firing at specific intervals are part of the given pattern. The pre-synaptic neurons that are not part of the pattern present randomly distributed Poisson noise. The network shown in Figure 3.2 is used to study the effect of radiation in this section. In that figure, $N_1$ to $N_{25/100}$ are pre-synaptic afferents and the post-synaptic afferent is represented by a leaky integrate circuit. Memristors ($M_1$ to $M_{25/100}$) in the circuit represent the synapses electrically connecting the pre-synaptic neurons with the post-synaptic LIF neuron. For simulation purposes, voltage sources mimic the behavior of the pre-synaptic afferents generating biphasic spikes.

### *Radiation with Limited Duration*

In this section, the memristor-based neural network that has partially learned the pattern is exposed to the state-altering radiation for a limited duration such as 10 to 40 s. the network's ability to keep learning or recovering the pattern post radiation is analyzed.

Figure 4.4 shows the change in the state of the 25-memristive devices in the neural network. The network is exposed to the state-altering radiation for 10 s after 30 s of learning the pattern representing the 25-pixel letter ‘B’. The memristors were exposed to differing radiation flux of (b) 1x$10^{10}$ $cm^{-2}s^{-1}$, (c) 3x$10^{10}$ $cm^{-2}s^{-1}$ and (d) 5x$10^{10}$ $cm^{-2}s^{-1}$ at a magnitude μ = 25 μA and σ = 12.5 μA for only 10 s.

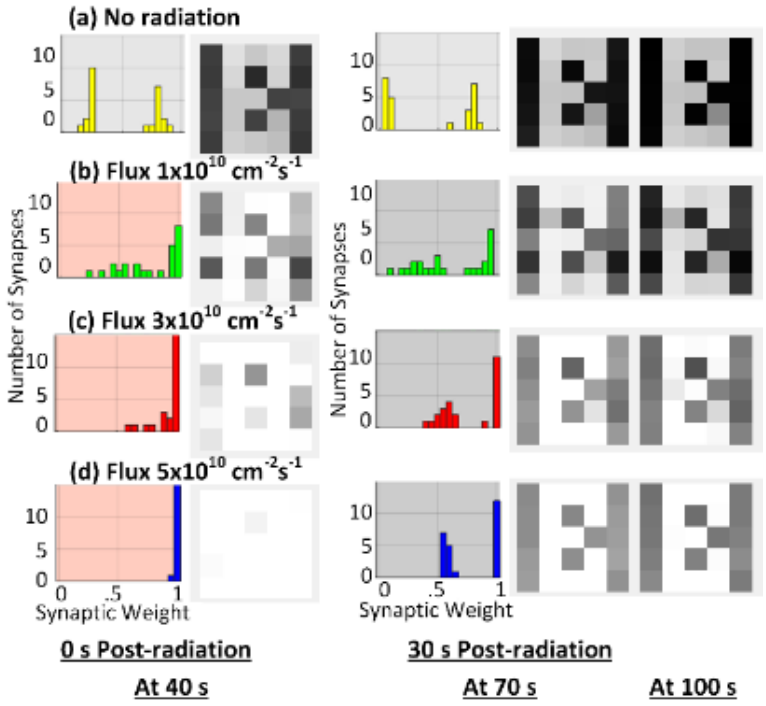


**Figure 4.4.** Memristors were exposed to 10 s of state-altering radiation (magnitude of 50 μA) at different flux after 30 s of learning is complete. As the flux increased, the pattern distorts and more saturation was observed in (d) at 40 s. The network was able to resolve the pattern but took a long time to stabilize at higher flux.

In Figure 4.4, the synaptic weight distribution is recorded right at the end of the radiation events (at 40 s) and at 70 s and 100 s as learning continued. It is observed that as the flux increases to $5x10^{10}$ $cm^{-2}s^{-1}$ , Figure 4.4d, the pattern completely disappears (at 0 s post-radiation). As pattern learning continues after the end of radiation, the system was able to relearn the pattern even in the case of intense radiation flux (Figure 4.4d). Although it did take much longer for the system to depress the non-participating afferents, the difference in synaptic weight distribution can be noted at 70 s and 100 s. Post-radiation (at 40 s) most of the synaptic weight seems to be biased towards $\frac{w}{D} = 1$ (more in Figure 4.4d than b) but as learning progresses at 70 s and 100 s the network was successfully able to depress the non-participating afferents and the system stabilizes again.

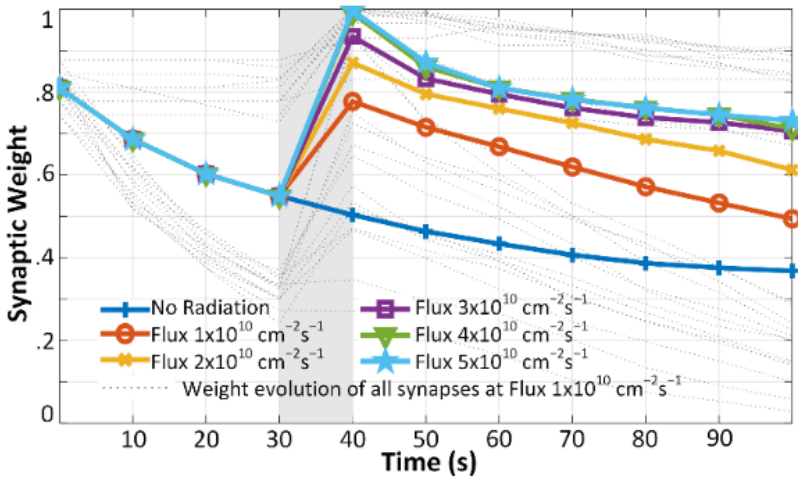


**Figure 4.5.** Evolution of the average synaptic-weight of all memristors at different flux. The network was exposed to state-altering radiation (magnitude 50 μA) for 10 s (grey area) after 30 s of learning. Post-radiation weights evolve toward the non-radiated weight curve as the network tries to resolve the pattern.

The evolution of the average synaptic weight of all 25 memristors is plotted in Figure 4.5. Irradiation of the system for 10 s starts at 30 s (grey region) at different flux with a mean pulse magnitude $\mu$ = 25 μA and standard deviation $\sigma$ = 12.5 μA. As expected, during the radiation events, the weights were climbing towards $\frac{w}{D} = 1$. At higher flux of $5x10^{10}$ $cm^{-2}s^{-1}$, all weights saturate post-radiation and the network is unable to recognize the pattern, as seen in Figure  at 40 s. At the end of radiation at 40 s, the mean weights start to evolve towards the non-radiated trace as the network tries to relearn the pattern. This indicates that the system is stabilizing itself by decreasing the average conductivity of the network, which was artificially increased due to the state-altering radiation event.

Figure 4.5 shows the synaptic weight distribution and pattern evolution, as the spiking neural network is in the process of learning a 100-pixel spatio-temporal pattern letter 'B'. Again, the network is exposed to 10 s of state-altering radiation (magnitude $\mu$ = 25 μA and $\sigma$ = 12.5 μA, starting at 30 s) at increasing flux. It is observed that as the flux increases, the pattern distortion also increases. This is because radiation is changing the state of the memristive synaptic devices and forcing them to be more conducive, as indicated by the STDP curve in Section 0. As the weights move toward more conductive states, the LIF post-synaptic neuron observes a stronger correlation and the system becomes unstable. For a neural network to be stable, synaptic weight distributions should look more like Figure 4.4a at 100 s, where the correlated weights are not completely saturated and therefore not over-simulating the LIF post-synaptic neurons, but contributing to the pattern.

At 40 s, after the end of the 10 s state-altering radiation event, the system tries to relearn the pattern, but the recovery does not necessarily result in the same pattern or a stable system. In the case of Figure 4.5d for flux $5x10^{10}$ $cm^{-2}s^{-1}$ at 40 s, the pattern is indistinguishable and post-radiation recovery left the system with a slightly different pattern and a relatively unstable synaptic weight balance. There are at least five pixels in this image (Figure 4.6d at 100 s) that are completely lost due to the radiation exposure (appear black instead of a light color).

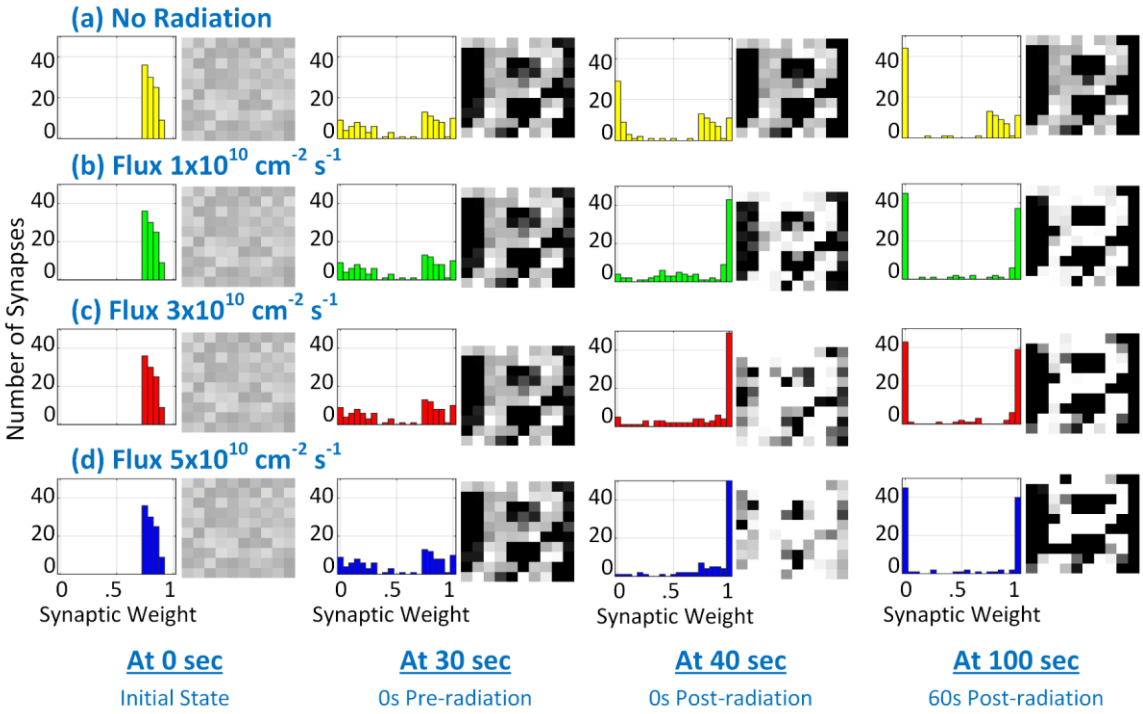


**Figure 4.6.** The synaptic weight distribution and pattern evolution over time as the system is exposed to 10 s (starting at 30 s) state-altering radiation (magnitude μ = 25 μA and σ = 12.5 μA) at increasing flux. The spiking neural network is in the process of learning a 100-pixel spatio-temporal pattern letter 'B'. As the flux increases, pattern distortion also increases. At $5x10^{10}$ $cm^{-2}s^{-1}$ flux, the pattern is completely indistinguishable at 40 s. Although the system tries to relearn the pattern after the end of radiation exposure, the recovery does not result in the same pattern or in a stable system.

Figure 4.7 shows a detailed analysis of data obtained from the 100 pre-synaptic neuron network simulation. Figure 4.7a plots the average synaptic weight evolution of all correlated and uncorrelated synapses separately over the 100 s period. During the radiation event (salmon color), uncorrelated synapses saw more deviation than correlated synapses. This effect is due to the non-linearity of the device. When it is less conductive, there is a larger change in synaptic weight compared to a highly conductive state.

It is also observed that the system became stable only after the average weight (calculated using Equation (4.1)) of the uncorrelated afferents slid lower than $0.1\,\frac{w}{D}$ (note dashed vertical lines in Figure 4.7a). Due to this, all the correlated synapses do not average out at the same value and result in a slightly different pattern as noted in Figure 4.6 at 100 s. This observation is clearer in Figure 4.7b where the cumulative variance (calculated using the Equation (4.2)) in a change of synaptic weight of correlated synapses stabilized after the vertical dashed lines confirming the system stability. As expected, the cumulative variance in weight change is higher for uncorrelated synapse at higher flux.

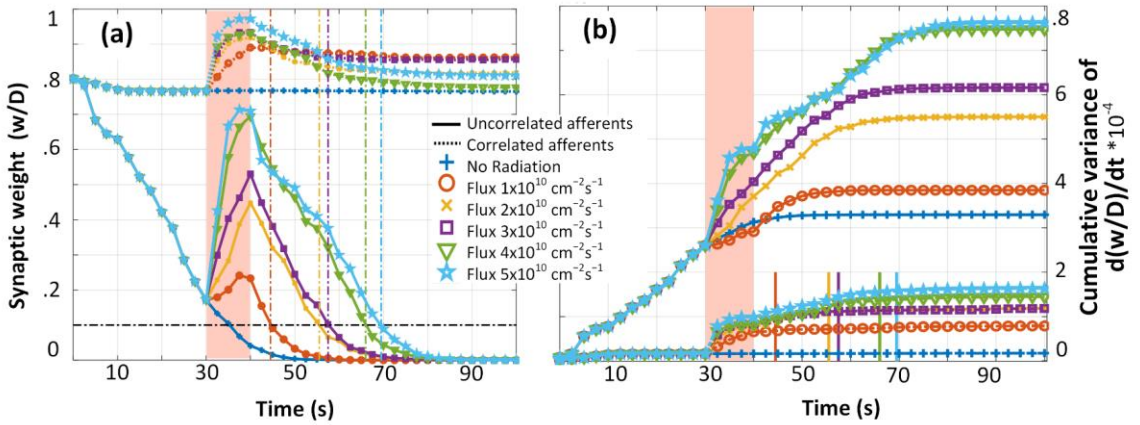


**Figure 4.7.** Network stability analysis of from the simulation in Figure 4.6. (a) Average and (b) cumulative variance in synaptic weight evolution of all correlated and uncorrelated synapses over 100 s period. In (a) during the radiation event (salmon color), uncorrelated synapses saw more deviation than correlated synapses and the system became stable only after the average weight of uncorrelated afferent slid lower than 0.1 value of $\frac{w}{D}$ (dashed vertical lines). This observation can be made more clearly in (b) where the cumulative variance in synaptic weight of correlated synapses stabilized after the vertical dashed lines.

The formulas used in the calculations are given as:

$$\text{Average weight}(n) = \frac{1}{n}\sum_{i=1}^{n}\left(\left(\frac{w}{D}\right)_i\right) \tag{4.1}$$

$$\text{Cumulative Variance of } \frac{d\left(\frac{w}{D}\right)}{dt}(n) = \sum_{i=1}^{n}\left(\left|\left(\frac{w}{D}\right)_i - (p)_i\right|\right) \tag{4.2}$$

$$\text{Mean Squared Error}\ (n) = \frac{1}{n}\sum_{i=1}^{n}\left(\left(\frac{w}{D}\right)_i - (p)_i\right)^2 \tag{4.3}$$

Where n is the total number of synaptic memristors under analysis (uncorrelated, correlated or all) and p is the desired weight of the corresponding synaptic device.

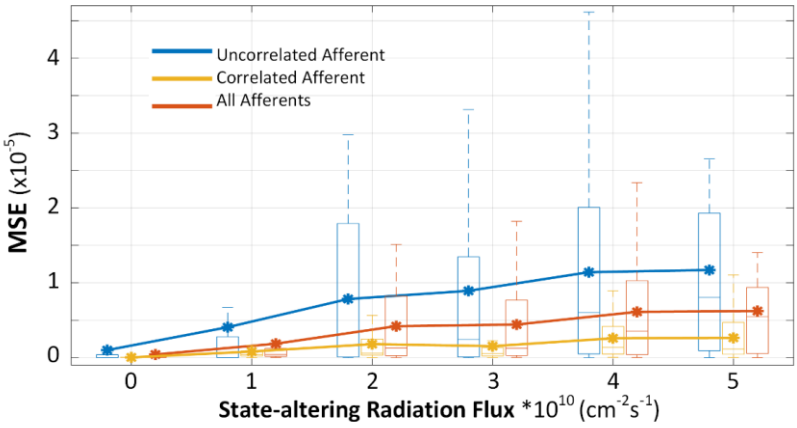


**Figure 4.8.** Error analysis of the network from the simulation in Figure 4.7. Box plot of mean squared error post-radiation (after 40 s) of uncorrelated, correlated and all synaptic weights. Note the increase in the average MSE and spread, as the radiation flux increases. The spread is more notable in uncorrelated synapses.

A box plot of mean squared error (MSE) of the post-radiation data (after 40 s) obtained from the same memristor-based 100 pre-synaptic Neuron network simulation is plotted in Figure 4.8. The MSE is calculated using Equation (4.3). The plot presents the simulations at different radiation flux for the synaptic weight of uncorrelated, correlated and all memristors ($M_1$ to $M_{100}$). As expected, the average MSE increases as the radiation increases and the box-whisker spread are significantly noticeable in the uncorrelated data set because it saw the most deviation during radiation, as seen in Figure 4.7a. Notably, the median of the radiated correlated data set is much closer to zero because this data set did not see much deviation during radiation due to the STDP $\frac{w}{D}$ non-linearity.

### *Learning in the Presence of Constant Radiation*

The simulation results shown in this section demonstrate the learning ability and the average synaptic weight evolution of the network in the presence of radiation of pulse magnitude $\mu = 0.5$ μA and $\sigma = 0.25$ μA at different flux. In these cases, radiation events started at 0 s when the network weight distribution. The goal of this experiment was to determine if the network can learn a pattern at all in the presence of radiation, or whether the weight evolutions are inevitably altered.

Figure 4.9 shows that until 40 s there was no major disruption in the network's ability to learn the pattern. Figure 4.9b at a lower flux of $1x10^{10}$ $cm^{-2}s^{-1}$ shows no visible change in the pattern recognition capability of the network for 100 s. It can be observed from Figure 4.9c, d, and e that as radiation flux increases, the network quickly becomes unstable sooner as radiation accumulates. It is interesting to note that in both Figure 4.9d and e, the network consistently and stably starts recognizing a different pattern again at 80 s.

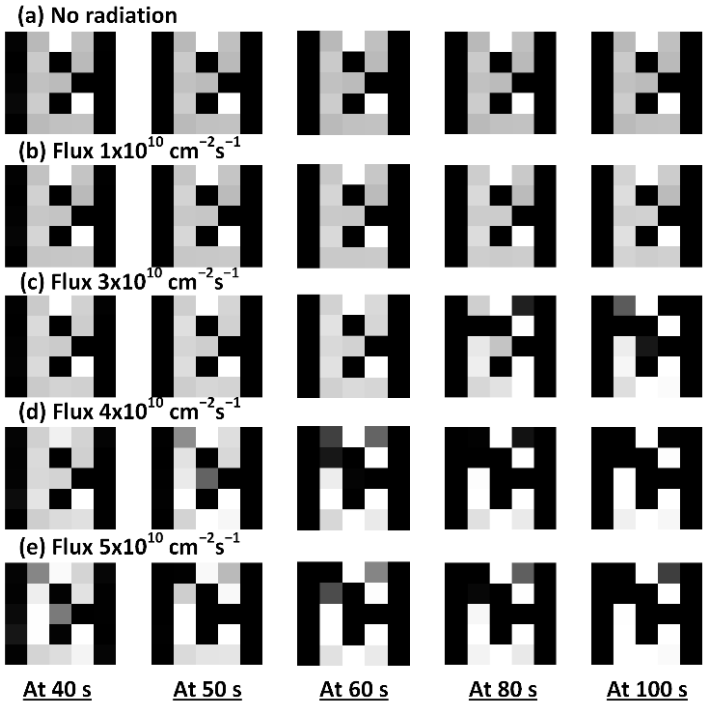


**Figure 4.9.** Memristors were exposed to state-altering radiation (flux magnitude μ = 0.5 μA and σ = 0.25 μA) throughout the learning process (for 100 s starting at 0 s). In each case the network was able to resolve the pattern in 40 s. Although, at higher flux (c), (d) and (e) the network became unstable at 80 s, 60 s, and 50 s. The network maintained the stability in (b) at the lower flux value.

A similar evolution can be noted in Figure 4.10, which plots the total average weight (calculated using Equation (4.1)) of all the afferent synapses versus time. In this plot, the weight evolution is similar until the flux reaches over $1x10^{10}$ $cm^{-2}s^{-1}$. Here, the flux weight evolution is similar to the no radiation curve, but higher flux causes a sudden decrease in total weight after 70 s, 50 s and 40 s in the case of $3x10^{10}$ $cm^{-2}s^{-1}$, $4x10^{10}$ $cm^{-2}s^{-1}$, and $5x10^{10}$ $cm^{-2}s^{-1}$ state-altering radiation flux. As observed in Figure 4.9d and e, Figure 4.10 also notes the stable evolution of weight after 70 s in both cases when the flux is at $4x10^{10}$ $cm^{-2}s^{-1}$, and $5x10^{10}$ $cm^{-2}s^{-1}$.

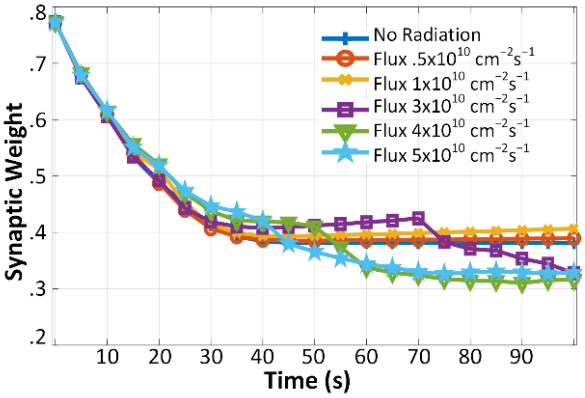


**Figure 4.10.** The average synaptic-weight evolution of all memristors as the network tries to learn the pattern in presence of state-altering radiation (for 100 s starting at 0 s) at different flux (pulse magnitude with μ = 0.5 μA and σ = 0.25 μA). The network tries to resolve the pattern but becomes unstable sooner as the flux increases. At a lower flux network was successfully able to recognize the pattern throughout the time.

Figure 4.11 shows the synaptic weight distribution and pattern evolution, as the spiking neural network is the process of learning the 100-pixel spatio-temporal pattern letter 'B'. The network is exposed to state-altering radiation (magnitude $\mu = 0.5$ μA and $\sigma = 0.25$ μA) at increasing flux up to $5x10^{10}$ $cm^{-2}s^{-1}$ throughout the learning process of 100 s. It can be noted in Figure 4.11 at $5x10^{10}$ $cm^{-2}s^{-1}$ flux at 100 s, correlated weights are pushed to the extreme, $\frac{w}{D} = 1$. Thus, LIF post-synaptic neuron starts over firing and the system becomes unstable and does not recognize the expected pattern. On the other hand, at $0.5x10^{10}$ $cm^{-2}s^{-1}$ flux, the system is very stable as the correlated weights are not saturated (LIF post-synaptic neuron is not over-stimulated) and the radiation is absorbed in the network.

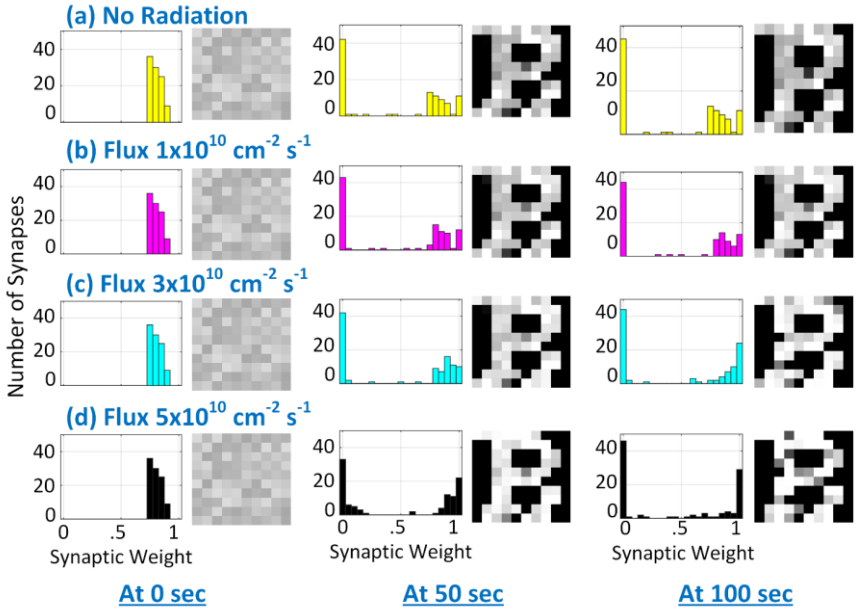


**Figure 4.11.** Shows the synaptic weight distribution and pattern evolution over time as the system is exposed to state-altering radiation (magnitude μ = 0.5 μA and σ = 0.25 μA) at increasing flux throughout the learning process of 100 s. The spiking neural network is in the process of learning a 100-pixel spatio-temporal pattern letter 'B'. As the flux increases, the system instability increases but at lower flux, the system was able to maintain stability.

Figure 4.12 shows the detailed analysis of data obtained from the network simulation shown in Figure 4.11. Figure 4.12a plots the average synaptic weight evolution of all correlated synapses over the 100 s period. At higher radiation, a deflection point can be observed (represented by the dotted horizontal black line). As the average correlated synaptic weight evolves to this point, the system becomes unstable. This observation can also be verified when the cumulative variance (calculated using Equation (4.2)) in the change of synaptic weight of the correlated afferent is plotted in Figure 4.11a. Note that the cumulative variance in weight keeps increasing after the deflection-point even though the system was relatively stable for flux $3x10^{10}$ $cm^{-2}s^{-1}$ and $4x10^{10}$ $cm^{-2}s^{-1}$ before the deflection.

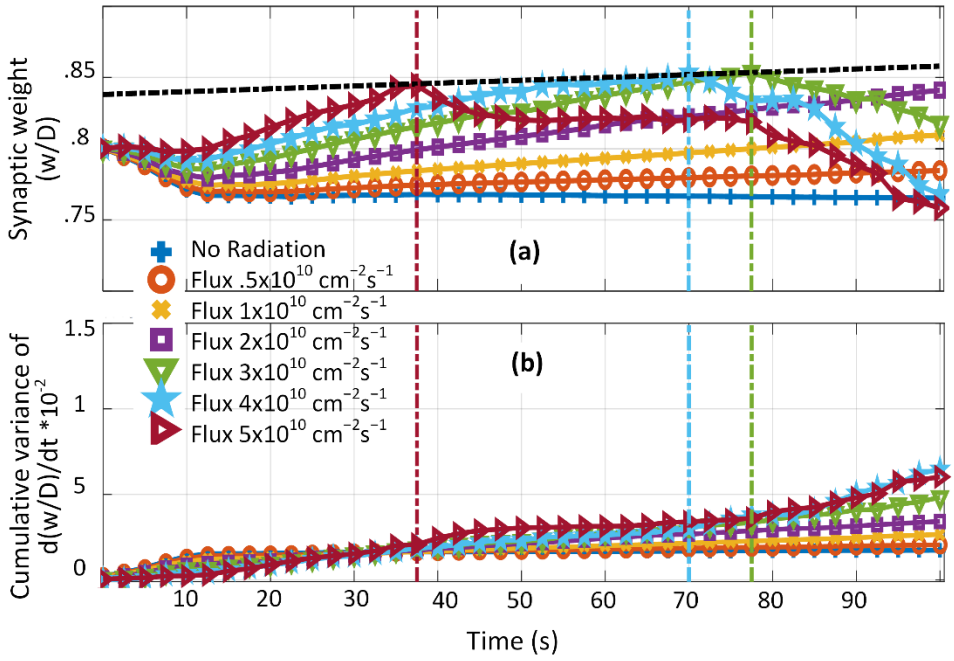


**Figure 4.12.** Stability analysis of simulated data captured in Figure 4.11. (a) Average synaptic weight and (b) Cumulative variance in the change of the synaptic weight of correlated synapses over 100 s period. In (a) at higher radiation, deflection point can be observed around $\frac{\mathbf{w}}{\mathbf{D}} = \mathbf{0.84}$, represented by the dotted horizontal black line, where the system become unstable. This observation is clearer in (b) where the cumulative variance in weight of correlated synapses destabilizes after the vertical dashed lines representing the respective deflection-points.

The MSE of $\frac{\mathrm{w}}{\mathrm{D}}$ data obtained from the network simulation in Figure 4.12 is plotted in Figure 4.13 at different radiation flux for synaptic weights of uncorrelated, correlated, and all memristors. Figure 4.13 plots the evolution of MSE overtime calculated using Equation (4.3). All synapses are initialized to a high conductance, thus the uncorrelated synapses (Figure 4.13a) started with the most error (MSE = 0.7) and as the network suppressed them the MSE reduced to 0. On the other hand, correlated synapses (Figure 4.13c) started with nearly zero MSE that increased over time as the system depressed and potentiated a few of the correlated synapses to attain stability. On average ( (Figure 4.13b), MSE decreased from 0.35 to 0.5 stably at lower radiation flux. On the other hand, as radiation flux increased, correlated synapses became unstable and MSE increased (Figure 4.13c).

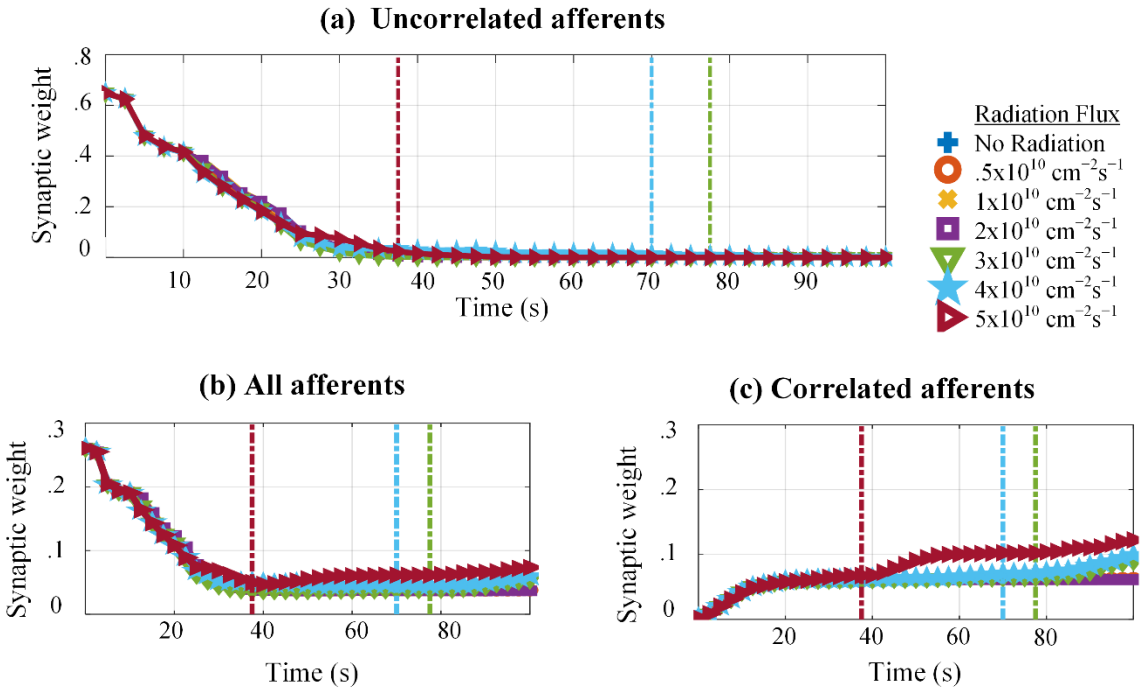


**Figure 4.13.** Mean Squared Error (MSE) analysis of network from the simulated data captured in Figure 4.11. MSE of (a) uncorrelated afferents, (b) all afferents, and (c) correlated afferents that are part of the pattern. On average MSE decreases at lower radiation flux but as radiation flux increases correlated synapses became unstable and MSE increases.

Figure 4.14 compares the distribution of MSE as the state-altering radiation flux increases from no radiation to $5x10^{10}$ $cm^{-2}s^{-1}$. As expected, the MSE increases as the radiation increases and the box-whisker spread is significantly noticeable at $4x10^{10}$ $cm^{-2}s^{-1}$ and $5x10^{10}$ $cm^{-2}s^{-1}$ as the system becomes more unstable due to weight saturation and LIF over-simulation. It is notable that the mean of the radiated correlated data set is almost stable until $3x10^{10}$ $cm^{-2}s^{-1}$, thus the system was able to absorb the radiation for 100 s until that flux.

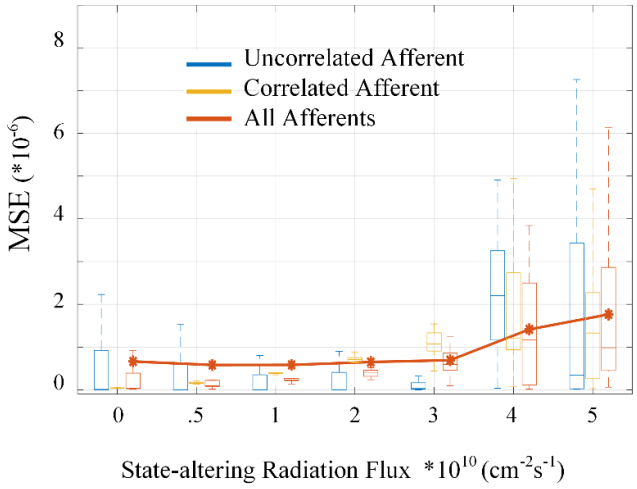


**Figure 4.14.** Box plot of MSE for 100 s of uncorrelated, correlated and all synaptic weights of the network from the simulated data captured in Figure 4.11. Note the average MSE does not increase for the lower flux and the spread increases only at much higher radiation flux.

### *Sensitivity Analysis and Network Stability*

The simulations provided in this section were performed without radiation to illustrate the challenges faced in terms of network stability. It will be critical to perform statistical analysis using many simulations with the same radiation profiles, but different timing and physical location within the network of the actual interactions. Figure 4.15 shows the synaptic weight evolutions of training the letter 'B' pattern as done previously with 10x10=100 pixels. The key point here is that minor variations in memristor behavior or initial synaptic weight distributions will change the trained filter (at 100 s), even for the exact same input signals. The memristor's activation threshold, or the voltage above which it will change state is clearly one critical parameter, and individual device variations may eventually play a major role in network evolution. There are likely to be other device variations (such as $R_{on}$ or $R_{off}$) that also effect training outcomes, although we have not yet looked into the sensitivity to those parameters.

Figure 4.16 shows synaptic weight evolutions in a different manner, in which the shaded regions correspond to presentation of spatio-temporal patterns. For the first 50 s of the 100 s transient simulations, the patterns are presented 100% of the time (just like in all previous examples). When the frequency of this presentation switches to 75%, 50%, and 25% (in Figure 4.16a, b, and c respectively), the network clearly becomes unstable the synaptic weights deviate rather quickly from their trained values. For the network in Figure 4.16c in particular, the rate of deviation is much faster than the other two cases, as observed by the slope of the synaptic weights for neurons that are participating in the pattern.


**Figure 4.15.** Synaptic weight evolutions of various simulations with three different inputs (sim 1, sim 2, and sim3), memristor thresholds, and initial memristor weight distributions (no radiation). Each was a 100 s transient simulation, trained on the black and white 'B' image shown at right. In the column labeled "At time: 100s", the trained filters are all different, even when the difference in parameters is very minimal.

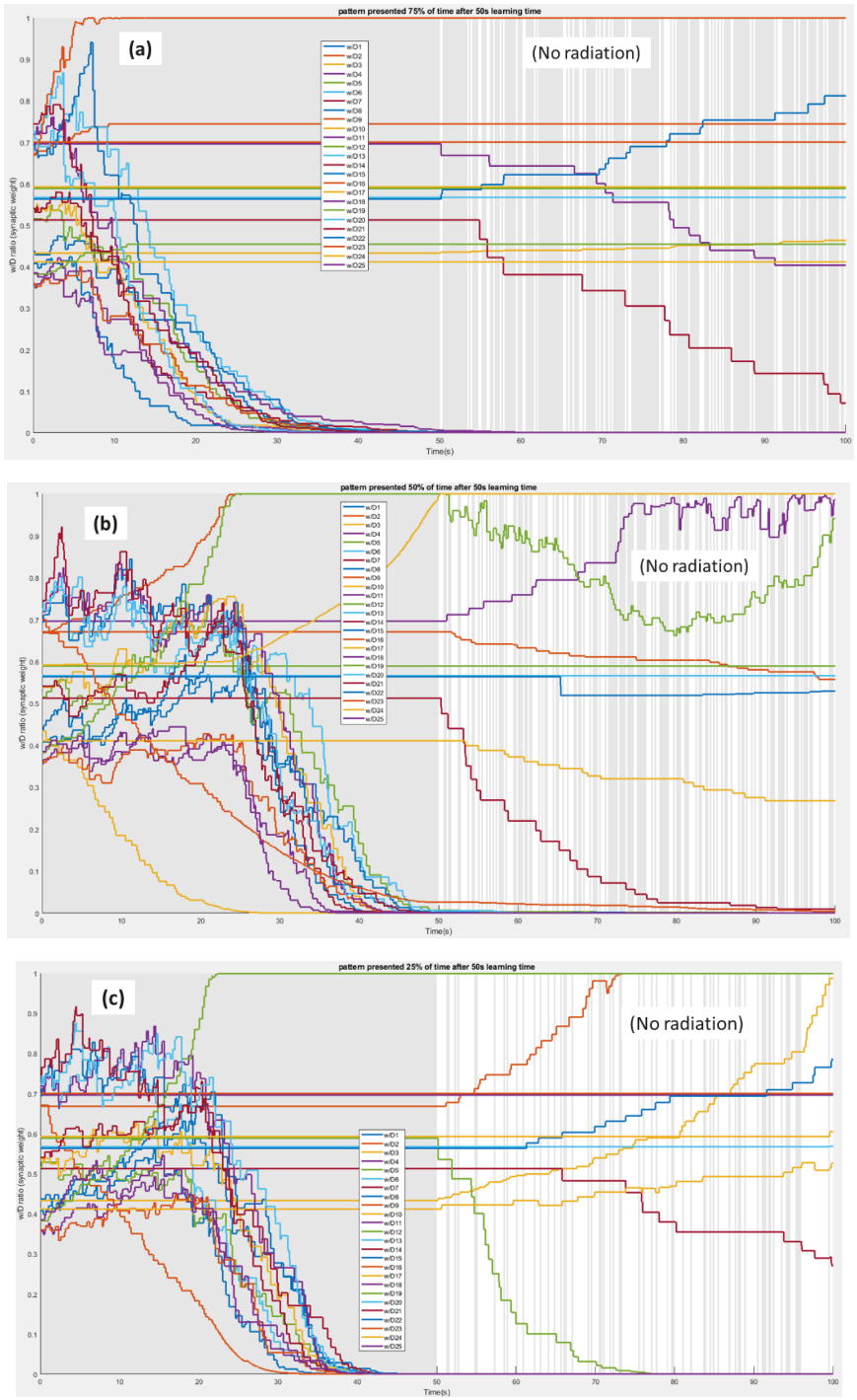


**Figure 4.16.** Three different synaptic weight evolutions in transient simulations of 100 s. In each case, the input signals and presented patterns are exactly the same for each afferent neuron. The only difference is the percentage of time in which the pattern is presented starting 50 s into the simulation. Namely, the weights are stable until the spatio-temporal pattern presentation frequency changes from 100% of the time to (a) 75% of the time (with all neurons in random Poisson mode 25% of the time), (b) 50% of the time, and (c) 25% of the time. It can be observed visually (from the weight evolutions slopes) that the network becomes less stable far more quickly in (c).

# 5. Effects of Neuron Failure

Neuron death occurs in biological neural networks (the brain) due to various reasons like aging, natural death during migration and differentiation, head injuries, spinal cord injuries, or neurodegenerative diseases. The cognitive functionality of the human brain gradually declines with age, leading to memory loss, learning slowdown, motor incoordination, and attention impairment [52], [53]. Neurodegenerative diseases also cause a considerable decline in neuron numbers. Parkinson's and Huntington's diseases lead to neuron death in the basal ganglia region of the brain and Alzheimer's affects the neurons in the neocortex and the hippocampus parts of the brain [52], [54], [55]. It generally takes about 60 years before people notice any measurable memory loss or become susceptible to develop neurodegenerative diseases [54]. Thus, the human brain demonstrates a remarkable ability to compensate for neuron losses over time, forestalling any noticeable effect until the losses become profound [53], [56]. According to one study from 1998, about 11 million people in the US experienced a stroke, of whom only approximately 0.77 million (7%) were symptomatic [57]. A vast majority of strokes are 'silent', although they can kill large numbers of cells rapidly [57]. Presently, the network-level effects of neuron death in electronic circuits is not addressed in the literature. This work contributes to filling that gap in the neuromorphic computing literature by analyzing the effect of neuron death in electronic SNNs.

Presently, shielding and hardening are common practices to protect devices and circuits from radiation, but these techniques are unable to block all particles from interacting with underlying electronics [63], [64]. Radiation in such cases can lead to neuron death due to circuit failure (CMOS: threshold shift, oxide breakdown, gate rupture, displacement damage [65], [66]) in the SNN. For this investigation, a memristor-based SNN is designed to learn a spatio-temporal pattern. The changes in the learning ability of the networks due to the death of the neurons are analyzed. In the neural network, synapses are realized using a memristor behavioral model. Although the presented network uses a single layer, the results can provide insight into the operation and response of the hidden layers within deep convolutional neural networks [67].

## 5.1 Simulation Setup

The neural network used for this part is shown in Figure 5.15.1 and consists of multiple pre-synaptic neurons, a post-synaptic neuron, and memristive synapses. It is the same network topology as the one shown in Figure 3.2, but where afferent neurons are lost due to radiation, instead of exposure at the synapses. This network mimics a single-layer perceptron network with 100 pre-synaptic afferents ($N_1$ to $N_{100}$), each connected to a single post-synaptic afferent via a single memristor ($M_1$ to $M_{100}$). The network uses biphasic shaped pulses to achieve pair-based STDP for pattern learning. Neuron death in the network is imitated by disabling pre-synaptic neurons randomly during the learning process.

Of the 100 pre-synaptic afferents, there are 60 participating/correlated (forming the part of letter B, brighter pixel, firing correlated spikes) and 40 non-participating/uncorrelated (not the part of letter B, darker pixel, firing uncorrelated spikes) afferents. A different percentages (up to 50%) of participating, non-participating, or random pre-synaptic neurons are turned off (killed) during the training to analyze the learning ability of the network.

In the initial setup, three neuron death cases are designed. The first case ("participating neuron dead") observes the changes in the pattern learning ability of the network when the random neurons that fail are all from the set of 60 participating neurons. The second ("non-participating neuron dead") is the case when the random neurons that fail are all from the set of 40 non-participating neurons. In the third case ("random neuron dead") failed neurons are picked randomly from the set of all 100 neurons. Neuron death is initiated at 30 s (instantaneous neuron death) when the network is in

a partially trained state. In each case, five sets of randomly chosen afferents are killed to improve the statistical validity of the conclusion.

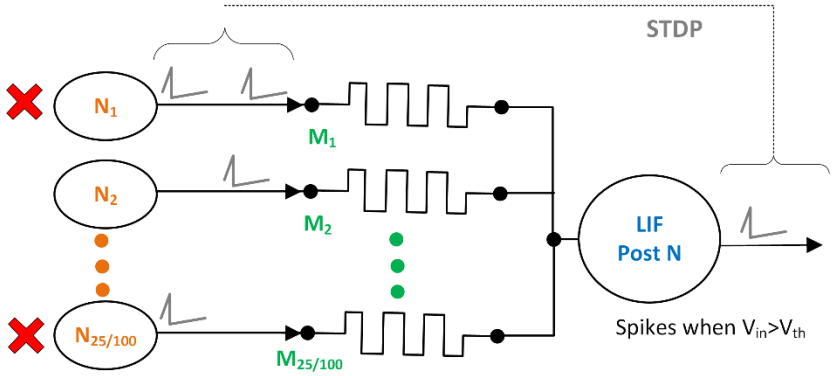


**Figure 5.1.** The memristor-based electronic Spiking Neural Network used for spatio-temporal pattern recognition. 25 or 100 pre-synaptic neurons are connected to one post-synaptic leaky integrate-and-fire (LIF) neuron via a single memristor each. The network uses biphasic shaped pulses to achieve pair-based STDP for pattern learning. Random neuron death is simulated by disconnecting pre-synaptic neurons after 30 s of partial learning.

A particular interest is comparing the differences in the learning ability of the network in the case when a given percentage of neurons die instantaneously at 30 s (instantaneous neuron death) versus slowly over time (gradual neuron death). Instantaneous death would occur in the case when a strong radiation flare may kill certain afferents all at the same time. On the other hand, if the radiation events are not strong but are spread over time like in the case of war zones and radiation accidents, the afferent will fail slowly and randomly for 30 s.

## 5.2 Neuron Death Simulation Results

### *No Neuron Death*

The neural network used has 100 pre-synaptic neurons with 60 participating (firing mutually correlated spikes ) and 40 non-participating (firing Poisson distributed uncorrelated spikes) afferents. Figure 5.2 shows the spiking characteristics of the 40 uncorrelated/non-participating pre-synaptic afferents individually and collectively over time. Figure 5.2a represents the firing times of 40 afferents for the first 20 s, with an obvious random firing distribution. Figure 5.2b shows the random distribution of firing frequency of each 40 uncorrelated afferents with a mean of 5 Hz. Figure 5.2c captures the firing frequency of all 40 non-participating over 100 s of stimulation, the frequency is measured over 1 s period (bin size).

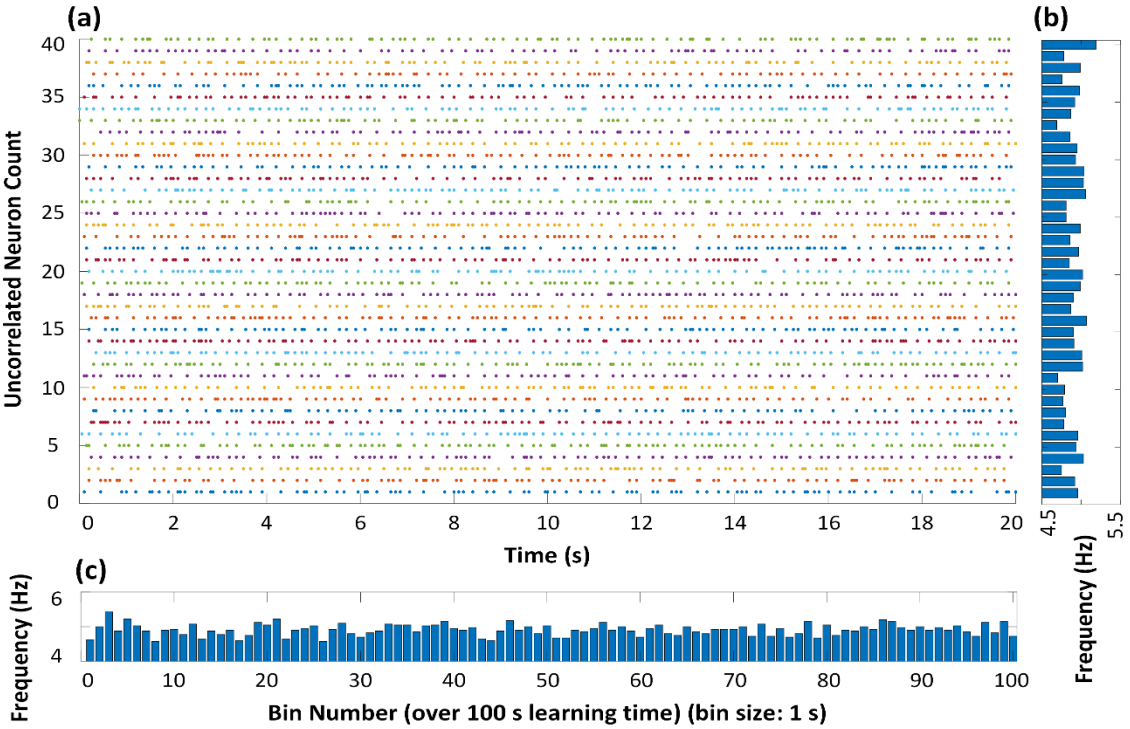


**Figure 5.2.** The random behavior of the 40 non-participating afferents. (a) The 20 s scatter plot of firing times of 40 (uncorrelated) afferents. (b) Random distribution of firing frequency of each of the 40 uncorrelated afferents with mean of 5 Hz. (c) Firing frequency of all 40 non-participating afferents over 100 s of stimulation, frequency is measured over 1 s period (bin size).

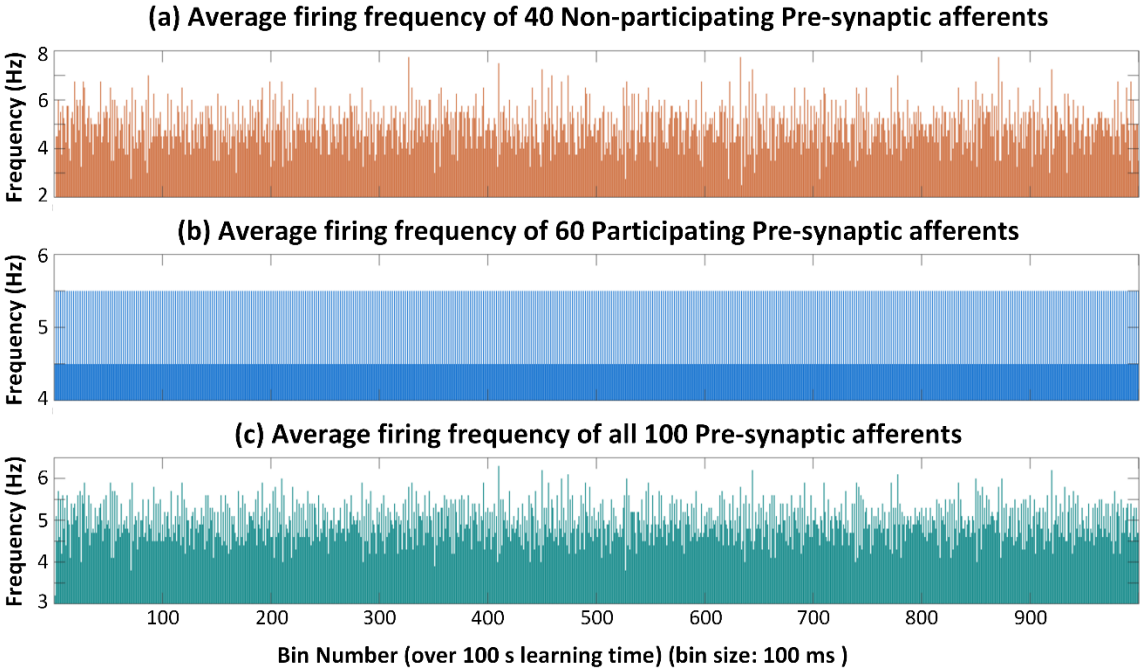


**Figure 5.3.** (a) Frequency distribution 40 non-participating afferents as they as fire Poisson distributed noise. (b) The frequency distribution of 60 participating afferents is not random as they are firing mutually correlated spikes. (c) Frequency distribution of the whole network over 100 s of the simulation.

Figure 5.3 presents the firing frequency of the network over 100 s of simulation. In this case, the frequency is measured over reduced 100 ms bins to observe the finer distribution. 40 non-participating afferents in Figure 5.3a display random frequencies, as they are firing Poisson distributed noise. On the other hand, the frequency distribution of 60 participating afferents in Figure 5.3b is not random because they are firing mutually correlated spikes at 5 Hz. However, their spike position within the 1 s window is random, as was illustrated by $N_{12}$ and $N_{13}$ in Figure 3.7a. Figure 5.3c shows the frequency distribution of the whole network over 100 s of the simulation. It can be noted that on average, the afferents are firing at the rate of 5 Hz.

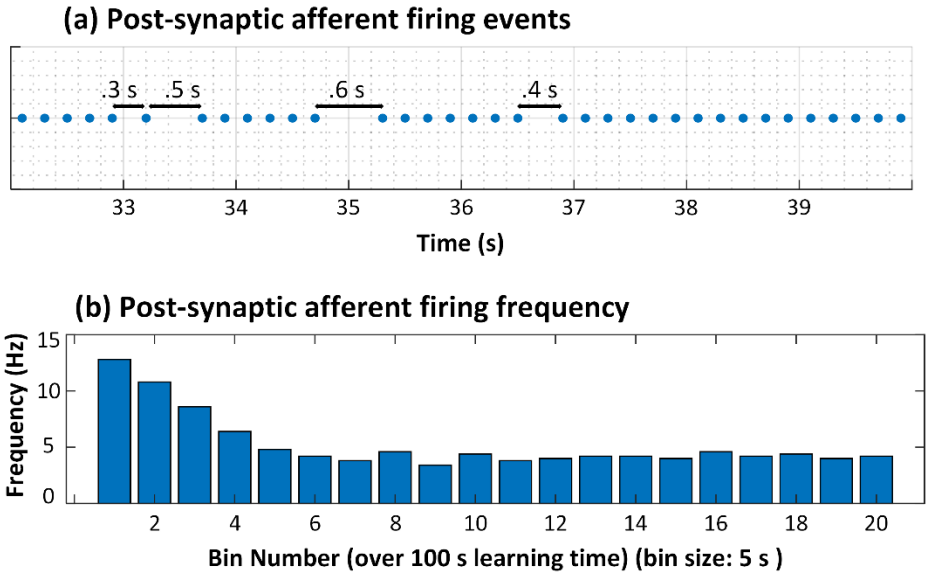


**Figure 5.4.** (a) The post-synaptic afferent is firing periodically every 0.2 s after 30 s except at a few misses (b) frequency response of the post-synaptic afferent over 100 s of simulation with a bin size of 5 s presenting the stabilized network over time to about 5 Hz, as non-participating afferents are suppressed.

Figure 5.4 shows the response of the post-synaptic LIF neuron during the 100 s learning period. As can be seen in Figure 5.4a, the post-synaptic afferent is firing periodically every 0.2 s after 30 s, except for a few misses of 0.3 s, 0.5 s, and 0.6 s. Figure 5.4b shows the frequency response over 100 s of simulation with a bin size of 5 s. Initially, the post-synaptic LIF neuron was overexcited due to high synaptic connectivity, but stabilized over time to about 5 Hz, as the network suppresses the non-participating afferents.

***Instantaneous Neuron Death***

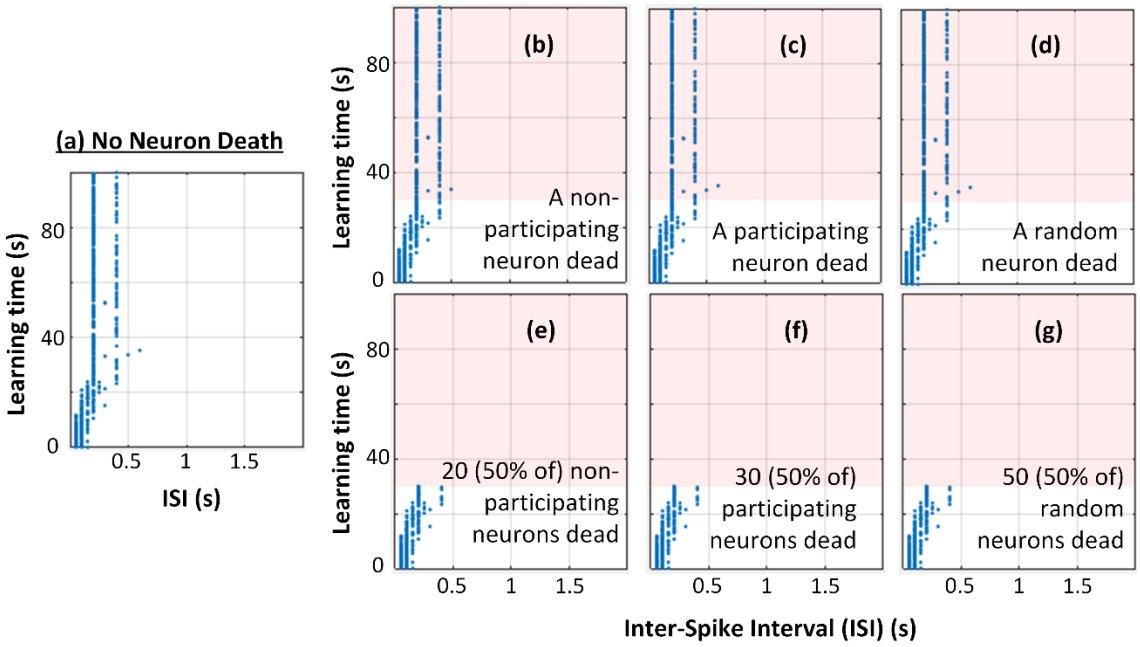


**Figure 5.5.** The post-synaptic neuron Inter Spike Interval (ISI) over the learning period. (a) ISI is about 0.2 s and 0.4 s in the case when no neuron death occurs. (b), (c) and (d) show the ISI when one neuron (in each case non-participating, participating and random) failed, but the network shows no degradation. (e), (f) and (g) present the ISI overtime when 50% of randomly selected afferents are dead and the network presents no post-synaptic neuron activity, thus resulting in complete network failure.

Figure 5.5 5.5a shows the Inter Spike Interval (ISI) between two spikes fired by the post-synaptic neuron, in the case when no neuron death occurs; the ISI is about 0.2 s and 0.4 s. Figure 5.5b, c, and d show the ISI when one neuron in each case of non-participating, participating, and random failed. ISI is still approximately 0.2 s and 0.4 s in each of the cases and no change in the pattern learning behavior of the network is observed. Figure 5.5e, f, and g present the ISI versus time when 50% of randomly selected afferents failed in each case of the non-participating, participating, and random. After the neuron death at 30 s, no spiking in the post-synaptic neuron is noted and the network was not able to learn the pattern in any of the cases.

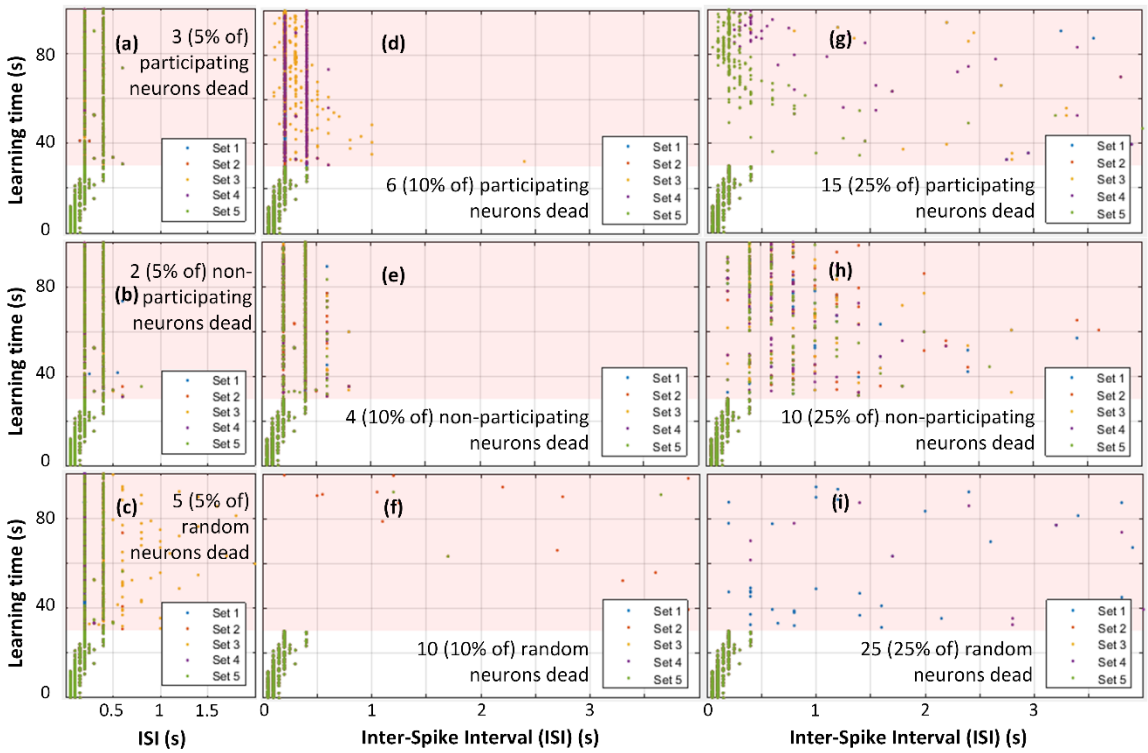


**Figure 5.6.** Post-synaptic neuron Inter Spike Interval (ISI) over the learning period. (a), (b), and (c) shows the ISI when 5% of randomly selected neurons (in each case of the non-participating, participating and random). The network was able to recover in the case of (a) and (b) but in the case of the random death, (c), the network recovery was not successful. (d), (e) and (f) presents the ISI over time when 10% of the randomly selected afferents are dead. (d), (e), and (f) ((g), (h), and (i)) presents the ISI over time when 10% (25%) of the randomly selected afferents are dead. The increase in network instability increases as the afferent death percentage increases, although random neuron death adds the most instability to the network.

Figure 5.6a, b, and c shows the ISI when 5% of the afferents in each case of the participating, non-participating, and random failed. Interestingly, in Figure 5.6a and b, where participating and non-participating neurons failed, the system did not destabilize like a random failure in Figure 5.6c, where the network instability is notable. Figure 5.6d, e, and f shows the ISI when 10% of the afferents in each case of the participating, non-participating, and random failed. It is observed that in Figure 5.6e, the non-participating afferent death keeps the system relatively stable. In the case of random neuron death, in Figure 5.6f, after 30 s, the post-synaptic neuron is not learning the pattern as the system becomes unstable and the ISI is randomly distributed. Similarly, Figure 5.6g, h, and i show the ISI of a post-synaptic neuron when 25% of the pre-synaptic afferents in each case of the participating, non-participating, and random failed. Random neuron death shows the most instability in this case as well. In each case, five different sets of randomly selected afferents are disabled (set 1 to set 5).

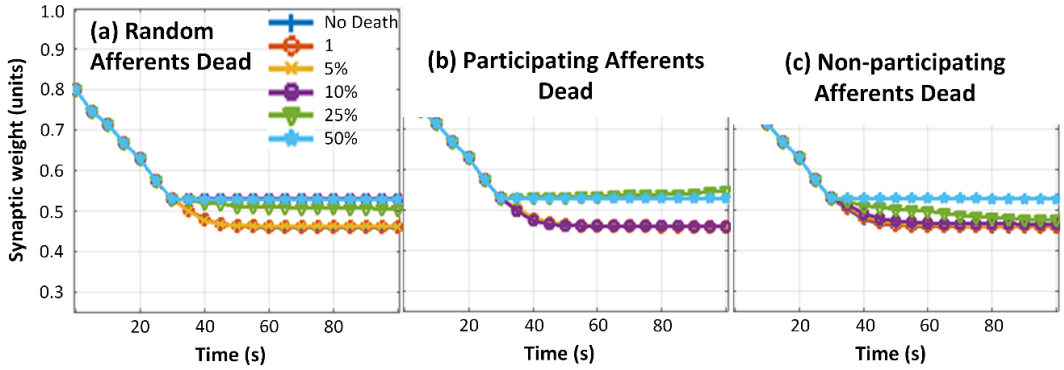


**Figure 5.7.** Normalized average synaptic weight evolution of all the 100 synaptic memristors in the network. (a) In the case of random afferent death, 10%, 25%, and 50% evolution show deviation from the no-death case. (b) In the case of random afferent death, 25% and 50% evolution shows deviation from the no-death case. (c) In the case of random afferent death, only 50% evolution shows deviation from the no-death case, and 25% recovers after an initial deviation, as the system tries to recover and regain stability.

Figure 5.7 5.7 shows the normalized average synaptic weight evolution of all the 100 synaptic memristors in the network. The deviation of weights was observed in the case of Random afferent death (Figure 5.7a) as 10%, 25%, and 50% evolutions show deviation from the no-death case. On the other hand, non-participating afferent death (Figure 5.7c) seems to destabilize the system the least, since even the 25% death marker evolves towards the more stable state to relearn the desired pattern.

### *Comparing Instantaneous and Gradual Neuron Death*

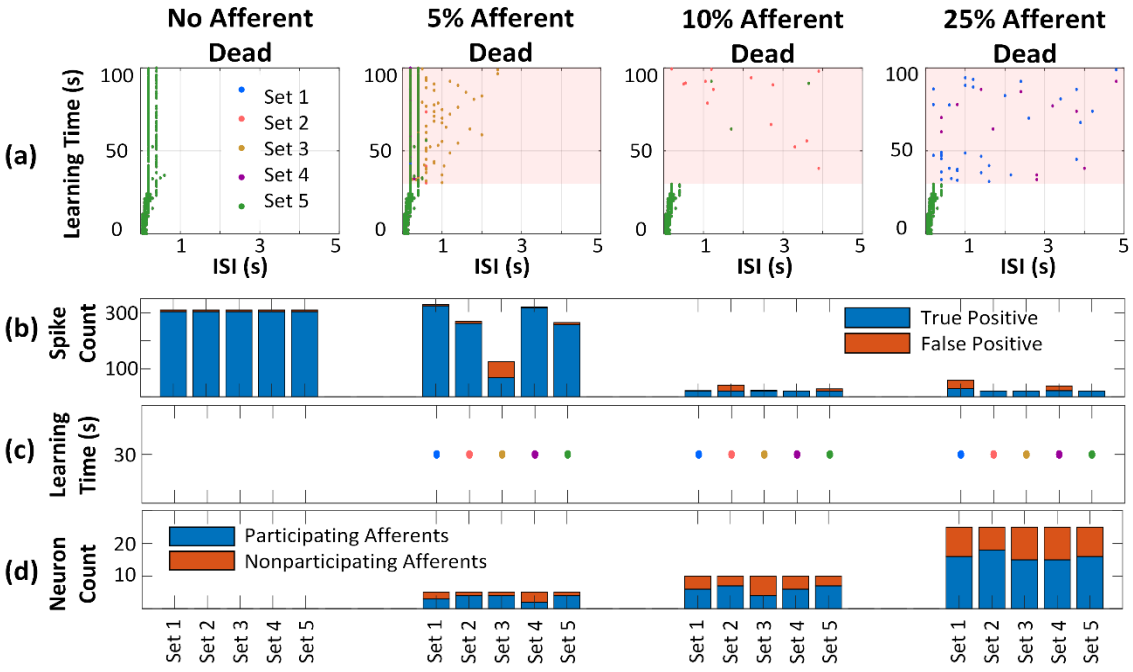


**Figure 5.8.** (a) post-synaptic afferent inter spiking interval over time, as the % of dead neurons increases, the network loses the pattern recognition capabilities. (b) the number of true positive and false positives recognized by the network, the network stops recognizing the pattern and the post-synaptic afferent stops firing as neuron death increases. (c) All afferents are dead instantaneously at 30 s. (d) The distribution of dead participating and non-participating afferents in each of the five sets in each case.

Figure 5.8 shows the analysis of the network when random neurons die at the same time after 30 s of learning. Figure 5.8a presents the post-synaptic afferent inter spiking interval over time, and as expected, as the percentage of dead neurons increases the network loses the pattern recognition capabilities. Figure 5.8b presents the number of true positive and false positives recognized by the network. As expected, as the percentage of dead neurons increases the network stops recognizing the pattern and the post-synaptic afferent stops firing. Figure 5.8c shows that the afferents are dead at 30 s and Figure 5.8d shows the distribution of dead participating and non-participating afferents in each of the five sets in each case.

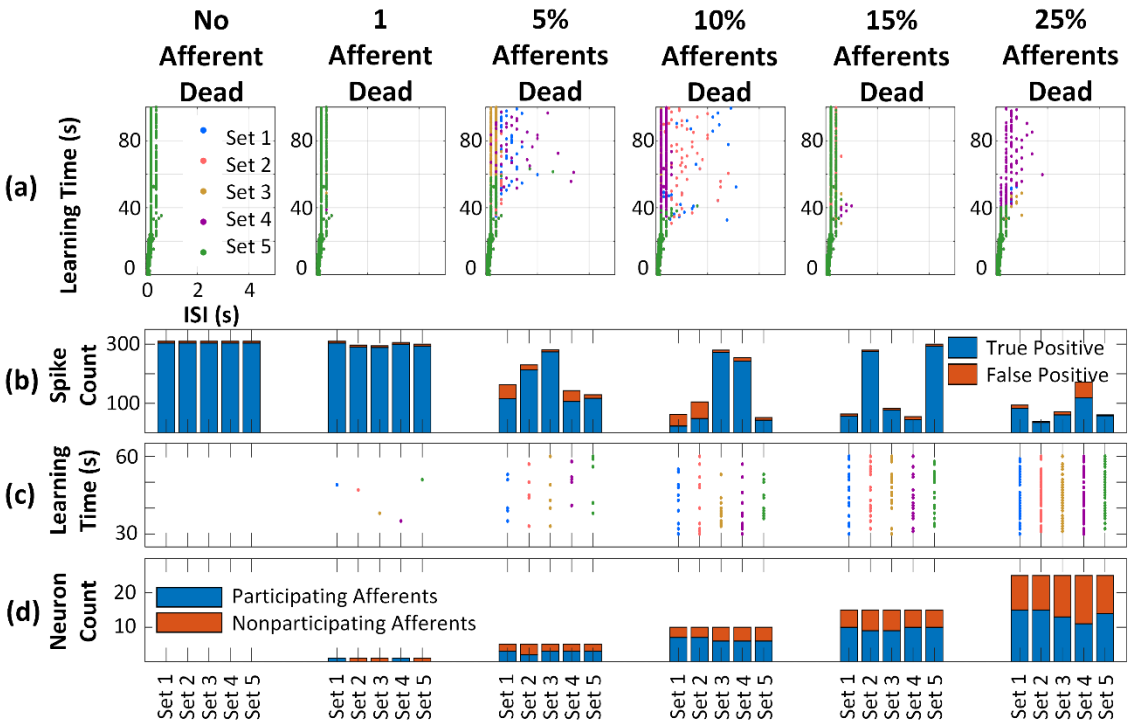


**Figure 5.9.** (a) post-synaptic afferent inter spiking interval over time, as the % of dead neurons increases the network loses the pattern recognition capabilities. (b) the number of true positives and false positives recognized by the network, the network stops recognizing the pattern and post-synaptic afferent stops firing as neuron death increases. (c) All afferents are dying randomly between 60 s and 30 s. (d) The distribution of dead participating and non-participating afferents in each of the five sets in each case.

Figure 5.9 shows a similar analysis of the network as Figure 5.8 except in this case the pre-synaptic neuron death time is randomly occurring, starting at 30 s until 60 s, as shown in Figure 5.9c. Figure 5.9a presents the post-synaptic afferent inter spiking interval over time and similarly shows the loss in the pattern recognition capabilities of the network as the percentage of dead neurons increases. Figure 5.9d shows the distribution of dead participating and non-participating afferents in each of the five sets in each case. Figure 5.9b presents the number of true positive and false positives recognized by the network.

Unlike in Figure 5.8, where instantaneous afferent death completely disabled the network, in Figure 5.9 a few sets were able to recover even in the case of high neuron death. Figure 5.9b shows a 10% neuron death, the network spiked well for set 3 and set 4 and even at 25% neuron death set 2 and set 5 did not harm the network strongly. On the other hand, in Figure 5.8b, the network did not perform well in the case of any of the simulated sets. Overall, the network learning performed better when the afferents failed gradually as compared to sudden death.

# 6. Conclusions and Future Work

The results of our research suggest that future memristor-based SNNs do have the potential to be incredibly defect-tolerant. In general, the devices themselves (memristors in particular) experience minimal degradation due to radiation. It seems likely that any long-term degradation that does occur can be mitigated at the network level. A particularly robust system will be one that is continuously learning and has some ability to retrain itself. However, even constant retraining does not always result in a perfect outcome, as evidenced by "lost" pixels described in Section 4.3.

## 6.1 Synaptic Modifications Caused by Radiation

A synaptic modification happens in the electronic SNNs when a radiation interaction event modifies the state of the memristive synapse. In this work, the STDP rule governs the learning capability of SNNs and is influenced by factors such as memristive synaptic device threshold, the initial state of the synaptic device, and the shape, size, and magnitude of the biphasic pulse across the memristor. Radiation events add asymmetry to the STDP curve forcing stronger potentiation and thus, adding instability in the network. It was concluded that when the network was not undergoing training, the radiation effects build up and accumulates in the network over time. On the other hand, the network can overcome the radiation effects when in the learning/training phase. Thus, hardware-based SNNs that are continuously learning such as in references [178]–[180] will survive better when exposed to radiation. The SNNs consist of one layer, designed to learn one feature. They are observed to be radiation resilient with minimal (if any) feature loss at the stronger flux of $3x10^{10}$ $cm^{-2}s^{-1}$ or higher. The larger multilayer deep neural networks that convolve multiple features and do not rely completely on one feature for object classification and identification should be more resilient to the effects of radiation, such as pixel upsets. Thus, future studies involving application-specific deep neural networks will help to understand the radiation effects in more detail. Further studies on different network architectures and topology will also provide more insight into the effects of radiation events on SNNs

## 6.2 Neuron Death

The simulations were designed to observe the effect on the learning ability of the network for three cases when selectively only participating neurons were affected, non-participating neurons were disabled, or random/non-selective neuron death occurred after 30 s into learning in the network. As expected, the network learning ability was least affected in the case when the non-participating afferents were disabled selectively. In this case, the network shows the capacity to recover even when 25% (10) of the non-participating afferents were killed off. On the other hand, when random/non-selective neuron death occurred in the network, the pattern learning ability degraded rapidly as 10% (10) of the total afferents were disabled and the network becomes unstable at 5% (5) neuron death. The chapter also simulated the case when neuron death is occurred gradually (instead of instantaneously at 30 s) between 30 s and 60 s of learning. The comparison shows that the network's learning ability was not as seriously deteriorated in the case of gradual neuron death as in the case of instantaneous death at 30 s. As the simulations show, in some of the cases of the gradual neuron death, the network was not affected by the neuron death. On the other hand, when all afferents die simultaneously at 30 s, the network did not recover.

The results conclude that the non-participating afferents contribute to improving the learning ability of the network even when partial learning is completed, emphasizing the importance of the non-participating neurons during the learning process. Instantaneous neuron death (due to radiation flare or a strong radiation event) will degrade the network's pattern recognition capability more than gradual neuron death (in the case of low but continuous radiation events, like in war zones, or post-

nuclear accident sites). Thus, the electronic spiking networks do present the capability to recover/retain their learning capability even in the case of random neuron death. Such cases of neuron death can be observed in radiation prone areas like space and war zones when electronic neurons might experience a failure due to one or more radiation events.

Neuron death occurs in electronic SNNs when one or more neurons in the network fail and become inactive due to degradation caused by radiation or general device/circuit failure. Section 5 concludes that SNNs apparently do have the ability to recover/retain their learned/trained pattern in case of neuron death. This ability is least affected when the non-participating afferents were disabled and most affected when the neuron both participating and non-participation afferent die randomly. In the larger multi-layer SNNs, every neuron is connected to multiple synapses. The network in this study shows that the instantaneous neuron death is more deteriorating for an SNN than gradual neuron death overtime. Thus, an optimally-connected network will be able to survive multiple gradual neuron deaths. Simulations also show that the non-participating afferents contribute to improving the learning ability of the network. More analysis is needed to understand the contribution of non-participating afferents. The study would help estimate the percentage of non-participating afferents needed for optimal learning and will also optimize the connection complexity in the larger networks.

## References


[1] D. Attwell and S. B. Laughlin, “An Energy Budget for Signaling in the Grey Matter of the Brain,” *J. Cereb. Blood Flow Metab.*, vol. 21, no. 10, pp. 1133–1145, 2001.

[2] J. Hawkins and S. Blakeslee, *On Intelligence*. New York: Henry Holt and Company, 2004.

[3] E. R. Kandel, J. H. Schwartz, and T. M. Jessell, *Principles of Neural Science*, Fourth. McGraw-Hill, 2000.

[4] B. Pakkenberg and H. J. G. Gundersen, “Neocortical neuron number in humans: Effect of sex and age,” *J. Comp. Neurol.*, vol. 384, no. 2, pp. 312–320, 1997.

[5] D. B. Strukov, G. S. Snider, D. R. Stewart, and R. S. Williams, “The missing memristor found,” *Nature*, vol. 453, no. 7191, pp. 80–83, 2008.

[6] Á.́ Rak and G. Cserey, “Macromodeling of the memristor in SPICE,” *IEEE Trans. Comput. Des. Integr. Circuits Syst.*, vol. 29, no. 4, pp. 632–636, 2010.

[7] S. Benderli and T. A. Wey, “On SPICE macromodelling of TiO2 memristors,” *Electron. Lett.*, vol. 45, no. 7, p. 377, 2009.

[8] S. Shin, K. Kim, and S.-M. Kang, “Compact Models for Memristors Based on Charge-Flux Constitutive Relationships,” *IEEE Trans. Comput. Des. Integr. Circuits Syst.*, vol. 29, no. 4, pp. 590–598, 2010.

[9] D. Batas and H. Fiedler, “A memristor SPICE implementation and a new approach for magnetic flux-controlled memristor modeling,” *IEEE Trans. Nanotechnol.*, vol. 10, no. 2, pp. 250–255, 2011.

[10] R. Kozma, R. E. Pino, and G. E. Pazienza, *Advances in neuromorphic memristor science and applications*. Springer, 2012.

[11] J. T. Diao and X. B. Tian, “A Simulation Method for Memristor Based Dopant Drift Model,” *Appl. Mech. Mater.*, vol. 239–240, no. December 2012, pp. 915–920, Dec. 2012.

[12] Y. Chen and X. Wang, “Compact modeling and corner analysis of spintronic memristor,” *2009 IEEE/ACM Int. Symp. Nanoscale Archit. NANOARCH 2009*, pp. 7–12, 2009.

[13] (Helen) Hai Li and M. Hu, “Compact model of memristors and its application in computing systems,” *Des. Autom. Test Eur. Conf. Exhib. (DATE), 2010*, pp. 673–678, 2010.

[14] M. Hu, H. Li, Y. Chen, X. Wang, and R. E. Pino, “Geometry variations analysis of TiO2thin-film and spintronic memristors,” *Proc. Asia South Pacific Des. Autom. Conf. ASP-DAC*, pp. 25–30, 2011.

[15] S. Kvatinsky, E. G. Friedman, A. Kolodny, and U. C. Weiser, “TEAM: Threshold adaptive memristor model,” *IEEE Trans. Circuits Syst. I Regul. Pap.*, vol. 60, no. 1, pp. 211–221, 2013.

[16] C. Yakopcic, S. Member, T. M. Taha, G. Subramanyam, S. Member, R. E. Pino, S. Member, and S. Rogers, “A Memristor Device Model,” *Electron Device Lett.*, vol. 32, no. 10, pp. 1436–1438, 2011.

[17] H. Abdalla and M. D. Pickett, “SPICE modeling of memristors,” in *IEEE International Symposium on Circuits and Systems (ISCAS)*, 2011, pp. 1832–1835.

[18] M. D. Pickett, D. B. Strukov, J. L. Borghetti, J. J. Yang, G. S. Snider, D. R. Stewart, and R. S. Williams, “Switching dynamics in titanium dioxide memristive devices,” *J. Appl. Phys.*, vol. 106, no. 7, pp. 1–6, 2009.

[19] Y. V. Pershin and M. Di Ventra, “SPICE model of memristive devices with threshold,” *Radioengineering*, vol. 22, no. 2, pp. 485–489, 2013.

[20] Z. Kolka, V. Biolkova, and D. Biolek, “Simplified SPICE model of TiO 2 memristor,” in *2015 International Conference on Memristive Systems (MEMRISYS)*, Nov. 2015, no. 3, pp. 1–2.

[21] S. G. Dahl, R. Ivans, and K. D. Cantley, “Modeling Memristor Radiation Interaction Events and the Effect on Neuromorphic Learning Circuits,” *Proc. Int. Conf. Neuromorphic Syst. - ICONS ’18*, pp. 1–8, 2018.

[22] M. Laiho, E. Lehtonen, A. M. T. Russell, and P. Dudek, “Memristive synapses are becoming reality,” *The Neuromorphic Engineer*, 2010.

[23] C. Yakopcic, T. M. Taha, G. Subramanyam, and R. E. Pino, “Generalized memristive device SPICE model and its application in circuit design,” *IEEE Trans. Comput. Des. Integr. Circuits Syst.*, vol. 32, no. 8, pp. 1201–1214, 2013.

[24] K. A. Campbell, “Self-directed channel memristor for high temperature operation,” *Microelectronics J.*, vol. 59, no. November 2016, pp. 10–14, 2017.

[25] R. E. Pino, J. W. Bohl, N. McDonald, B. Wysocki, P. Rozwood, K. A. Campbell, A. Oblea, and A. Timilsina, “Compact method for modeling and simulation of memristor devices: Ion conductor chalcogenide-based memristor devices,” *Proc. 2010 IEEE/ACM Int. Symp. Nanoscale Archit. NANOARCH 2010*, pp. 1–4, 2010.

[26] E. Deionno, M. D. Looper, J. V. Osborn, H. J. Barnaby, and W. M. Tong, “Radiation effects studies on thin film TiO2 memristor devices,” *IEEE Aerosp. Conf. Proc.*, pp. 1–8, 2013.

[27] W. M. Tong, J. J. Yang, P. J. Kuekes, D. R. Stewart, R. S. Williams, E. DeIonno, E. E. King, S. C. Witczak, M. D. Looper, and J. V. Osborn, “Radiation hardness of TiO2 memristive junctions,” *IEEE Trans. Nucl. Sci.*, vol. 57, no. 3 PART 3, pp. 1640–1643, 2010.

[28] E. Deionno, M. D. Looper, J. V. Osborn, and J. W. Palko, “Displacement damage in Tio2 Memristor devices,” *IEEE Trans. Nucl. Sci.*, vol. 60, no. 2, pp. 1379–1383, 2013.

[29] S. P. Adhikari, C. Yang, H. Kim, and L. O. Chua, “Memristor bridge synapse-based neural network and its learning,” *IEEE Trans. Neural Networks Learn. Syst.*, vol. 23, no. 9, pp. 1426–1435, 2012.

[30] K. D. Cantley, A. Subramaniam, H. J. Stiegler, R. A. Chapman, and E. M. Vogel, “Hebbian learning in spiking neural networks with nanocrystalline silicon TFTs and memristive synapses,” *IEEE Trans. Nanotechnol.*, vol. 10, no. 5, pp. 1066–1073, 2011.

[31] K. D. Cantley, A. Subramaniam, H. J. Stiegler, R. A. Chapman, and E. M. Vogel, “Neural

Learning Circuits Utilizing Nano-Crystalline Silicon Transistors and Memristors," *IEEE Trans. Neural Networks Learn. Syst.*, vol. 23, no. 4, pp. 565–573, Apr. 2012.

[32] N. R. Mcdonald, R. E. Pino, S. Member, B. T. Wysocki, and P. J. Rozwood, "Analysis of Dynamic Linear and Non-linear Memristor Device," 2010.

[33] T. Prodromakis, P. Boon Pin, C. Papavassiliou, and C. Toumazou, "A Versatile Memristor Model With Nonlinear Dopant Kinetics," *IEEE Trans. Electron Devices*, vol. 58, no. 9, pp. 3099–3105, 2011.

[34] Y. N. Joglekar and S. J. Wolf, "The elusive memristor: Properties of basic electrical circuits," *Eur. J. Phys.*, vol. 30, no. 4, pp. 661–675, 2009.

[35] Z. Biolek, D. Biolek, and V. Biolková, "SPICE model of memristor with nonlinear dopant drift," *Radioengineering*, vol. 18, no. 2, pp. 210–214, 2009.

[36] J. Yu, X. Mu, X. Xi, and S. Wang, "A Memristor Model with Piecewise Window Function," 2013.

[37] L. Chua, "If it's pinched it's a memristor," *Memristors Memristive Syst.*, vol. 9781461490, pp. 17–90, 2014.

[38] M. L. McLain, H. P. Hjalmarson, T. J. Sheridan, P. R. Mickel, D. Hanson, K. McDonald, D. R. Hughart, and M. J. Marinella, "The susceptibility of TaOx-based memristors to high dose rate ionizing radiation and total ionizing dose," *IEEE Trans. Nucl. Sci.*, vol. 61, no. 6, pp. 2997–3004, 2014.

[39] J. L. Taggart, Y. Gonzalez-Velo, D. Mahalanabis, A. Mahmud, H. J. Barnaby, M. N. Kozicki, K. E. Holbert, M. Mitkova, K. Wolf, E. Deionno, and A. L. White, "Ionizing radiation effects on nonvolatile memory properties of programmable metallization cells," *IEEE Trans. Nucl. Sci.*, vol. 61, no. 6, pp. 2985–2990, 2014.

[40] B. Butcher, X. He, M. Huang, Y. Wang, Q. Liu, H. Lv, M. Liu, and W. Wang, "Proton-based total-dose irradiation effects on Cu/HfO2:Cu/Pt ReRAM devices," *Nanotechnology*, vol. 21, no. 47, p. 475206, 2010.

[41] M. J. Marinella, S. M. Dalton, P. R. Mickel, P. E. D. Dodd, M. R. Shaneyfelt, E. Bielejec, G. Vizkelethy, and P. G. Kotula, "Initial Assessment of the Effects of Radiation on the Electrical Characteristics of Memristive Memories," *Nucl. Sci. IEEE Trans.*, vol. 59, no. 6, pp. 2987–2994, 2012.

[42] H. J. Barnaby, S. Malley, M. Land, S. Charnicki, A. Kathuria, B. Wilkens, E. Deionno, and W. M. Tong, "Impact of alpha particles on the electrical characteristics of TiO 2 memristors," *IEEE Trans. Nucl. Sci.*, vol. 58, no. 6 PART 1, pp. 2838–2844, 2011.

[43] L. F. Abbott and S. B. Nelson, "Synaptic Plasticity: Taming the Beast," *Nat. Neurosci.*, vol. 3, pp. 1178–1183, 2000.

[44] G. Bi and M. Poo, "Synaptic Modification by Correlated Activity: Hebb's Postulate Revisited," *Annu. Rev. Neurosci.*, vol. 24, pp. 139–166, 2001.

[45] T. Serrano-Gotarredona, T. Masquelier, T. Prodromakis, G. Indiveri, and B. Linares-Barranco, "STDP and STDP variations with memristors for spiking neuromorphic learning systems," *Front. Neurosci.*, vol. 7, no. 2, pp. 1–15, 2013.

[46] N. Panwar, B. Rajendran, and U. Ganguly, “Arbitrary Spike Time Dependent Plasticity (STDP) in memristor by analog waveform engineering,” *IEEE Electron Device Lett.*, vol. 38, no. 6, pp. 740–743, 2017.

[47] J. Lisman and N. Spruston, “Questions About STDP as a General Model of Synaptic Plasticity,” *Front. Synaptic Neurosci.*, vol. 2, no. 140, 2010.

[48] R. C. Ivans, K. D. Cantley, E. M. Vogel, R. C. Ivans, A. Subramaniam, and E. M. Vogel, “Spatio-Temporal Pattern Recognition in Neural Circuits with Memory-Transistor-Driven Memristive Synapses,” in *2017 International Joint Conference on Neural Networks (IJCNN)*, 2017, pp. 4633–4640.

[49] S. Wozniak, T. Tuma, A. Pantazi, and E. Eleftheriou, “Learning spatio-temporal patterns in the presence of input noise using phase-change memristors,” *Proc. - IEEE Int. Symp. Circuits Syst.*, vol. 2016-July, pp. 365–368, May 2016.

[50] S. G. Dahl and K. D. Cantley, “Radiation Effect on Learning Behavior in Memristor-Based Neuromorphic Circuit,” in *IEEE International Midwest Symposium on Circuits and Systems –MWSCAS’19*, 2019.

[51] S. G. Dahl, R. C. Ivans, and K. D. Cantley, “Learning Behavior of Memristor-Based Neuromorphic Circuits in the Presence of Radiation,” in *International Conference on Neuromorphic Systems - ICONS ’19 (under Rev.).*

[52] J. H. Morrison and P. R. Hof, “Life and death of neurons in the aging brain,” *Science (80-. ).*, vol. 278, no. 5337, pp. 412–419, Oct. 1997.

[53] D. G. T. Barrett, S. Denève, and C. K. Machens, “Optimal compensation for neuron loss,” *Elife*, vol. 5, no. DECEMBER2016, Dec. 2016.

[54] V. Castelli, E. Benedetti, A. Antonosante, M. Catanesi, G. Pitari, R. Ippoliti, A. Cimini, and M. d’Angelo, “Neuronal cells rearrangement during aging and neurodegenerative disease: Metabolism, oxidative stress and organelles dynamic,” *Frontiers in Molecular Neuroscience*, vol. 12. Frontiers Media S.A., p. 132, May 2019.

[55] R. D. Terry, E. Masliah, D. P. Salmon, N. Butters, R. DeTeresa, R. Hill, L. A. Hansen, and R. Katzman, “Physical basis of cognitive alterations in alzheimer’s disease: Synapse loss is the major correlate of cognitive impairment,” *Ann. Neurol.*, vol. 30, no. 4, pp. 572–580, Oct. 1991.

[56] N. Li, K. Daie, K. Svoboda, and S. Druckmann, “Robust neuronal dynamics in premotor cortex during motor planning,” *Nature*, vol. 532, no. 7600, pp. 459–464, Apr. 2016.

[57] M. C. Leary and J. L. Saver, “Annual Incidence of First Silent Stroke in the United States: A Preliminary Estimate,” *Cerebrovasc. Dis.*, vol. 16, no. 3, pp. 280–285, 2003.

[58] V. S. Kumar, J. Prasad, V. L. Narasimhan, and S. Ravi, “Application of artificial neural networks for prediction of solar radiation for Botswana,” in *2017 International Conference on Energy, Communication, Data Analytics and Soft Computing (ICECDS)*, Aug. 2017, pp. 3493–3501.

[59] A. Dmitriev, Y. Minaeva, Y. Orlov, I. Persiantsev, A. Suvorova, and I. Veselovsky, “Artificial Neural Network Applications to the Space Radiation Environment Modelling and Forecasting,” in *ESA Workshop on Space Weather*, 1999, pp. 393–397.

[60] “Artificial Intelligence and the Military | RealClearDefense.” .

[61] “Kalashnikov develops fully automated neural network-based combat module — RT World News.” .

[62] T. V. Santosh, G. Vinod, R. K. Saraf, A. K. Ghosh, and H. S. Kushwaha, “Application of artificial neural networks to nuclear power plant transient diagnosis,” *Reliab. Eng. Syst. Saf.*, vol. 92, no. 10, pp. 1468–1472, Oct. 2007.

[63] A. S. Keys, J. H. Adams, J. D. Cressler, R. C. Darty, M. A. Johnson, and M. C. Patrick, “High-performance, radiation-hardened electronics for space and lunar environments,” *AIP Conf. Proc.*, vol. 969, pp. 749–756, 2008.

[64] P. E. Dodd, M. R. Shaneyfelt, J. R. Schwank, and J. A. Felix, “Current and future challenges in radiation effects on CMOS electronics,” *IEEE Trans. Nucl. Sci.*, vol. 57, no. 4 PART 1, pp. 1747–1763, 2010.

[65] R. A. Burghard and C. W. Gwyn, “Radiation failure modes in CMOS integrated circuits,” *IEEE Trans. Nucl. Sci.*, vol. 20, no. 6, pp. 300–306, 1973.

[66] A. Paccagnella, A. Cester, and G. Cellere, “Ionizing radiation effects on MOSFET thin and ultra-thin gate oxides,” in *Technical Digest - International Electron Devices Meeting, IEDM*, 2004, pp. 473–476.

[67] S. Reza, M. Ganjtabesh, and S. J. Thorpe, “STDP-based spiking deep convolutional neural networks for object recognition,” *Neural Networks*, vol. 99, pp. 56–67, 2018.

# Appendix A – Non-Linear Memristor Models

## A.1 Model Without Radiation Effects

```
// Verilog-A code for non-linear memristor model (Vth and window function included)
`include "constants.vams"
`include "disciplines.vams"

// Take care of current blowup error
nature Current
   abstol = 1e-14 ;
        access = I ;
        units = "A" ;
        blowup = 1e12 ;
endnature

// Start of the module
module memristor_verilog_neurolearning(In, Out, w_D, RinitK, Vth);
input IRad_sc, RinitK, Vth;
output w_D;
inout In, Out;

electrical In, Out, w_D , capaux, capgnd, IRad_sc, RinitK, Vth;
branch (In, Out) mem;
branch (capgnd, capaux) cap;

parameter real Roff = 100k ;          //off-resistance in Ohms
parameter real Ron = 10k ;            //on-resistance in Ohms
parameter real D = 10n ;              //thickness of device in m
parameter real mu = 10f ;             //dopant ion mobility in m2/V s

real Gxconst, initcapV, Rhigh,Rinit,Vthp,Vthn,var,a,capv;   //variables used

// Start of the analog
analog begin
        Rhigh = Roff ;
        Vthp = 1* V(Vth);             // positive Vth
        Vthn = -1*V(Vth);             // negative Vth
        Rinit = 1000* V(RinitK);      // initial device state if defined externally by user
        //a = 45 + (abs( $random%30));              // generate random Rinit,
        //  Rinit = 1000* a;

        initcapV = (Rinit-Ron)/(Rhigh-Ron);        //initial voltage across capacitor
        Gxconst = mu*Ron/(D*D);             //Gx = Gxconst*Imem*window function
```

```
// Start of the analysis
if (analysis("ic"))begin                    // to reflect the initial state of the device
        V(cap) <+ initcapV ;                //initializing capacitor to initial state
        Capv = V(cap);

end else begin
        V(capgnd) <+ 0;
        I(cap) <+ ddt(V(cap));              //current contribution from cap

 //including Vthn and Vthp, to include threshold to the device
        if  ((V(mem) > Vthp) || (V(mem) < Vthn)) begin
                //adding the window function
                I(capaux) <+ Gxconst*I(mem) *(1-(pow(((2*V(cap))-1),8)));
        end

end     // End of the analysis

//check the boundary conditions
if(V(cap) >= 1)   V(cap) <+1;
if(V(cap) <= 0)    V(cap) <+0;

V(w_D) <+ V(cap);                           //state (w/D) of the memristor
V(mem) <+ I(mem)* ((Rhigh) -( Rhigh - Ron)* V(cap));
                                    //voltage across the memristor, V(mem) = V*Roff+Emem

end             // End of the analog
endmodule       // End of the module
```

**A.2 Model Including Radiation Effects**

```
// Verilog-A code for non-linear memristor model with state change radiation
`include "constants.vams"
`include "disciplines.vams"

// Take care of current blowup error
nature Current
   abstol = 1e-14 ;
        access = I ;
        units = "A" ;
        blowup = 1e12 ;
endnature

// Start of the module
module memristor_verilog_neurolearning_rad(In, Out, w_D, IRad_sc, RinitK, Vth);
input IRad_sc, RinitK, Vth;
```

```
output w_D;
inout In, Out;

electrical In, Out, w_D , capaux, capgnd, IRad_sc, RinitK, Vth;
branch (In, Out) mem;
branch (capgnd, capaux) cap;

parameter real Roff = 100k ;          //off-resistance in Ohms
parameter real Ron = 10k ;            //on-resistance in Ohms
parameter real D = 10n ;              //thickness of device in m
parameter real mu = 10f ;             //dopant ion mobility in m2/V s

real Gxconst, initcapV, Rhigh,Rinit,Vthp,Vthn,var,a,capv;   //variables used

// Start of the analog
analog begin
        Rhigh = Roff ;
        Vthp = 1* V(Vth);             // positive Vth
        Vthn = -1*V(Vth);             // negative Vth
        Rinit = 1000* V(RinitK);      // initial device state if defined externally by user
//a=45+ (abs( $random%30));           // generate random Rinit,
//  Rinit = 1000* a;

        initcapV = (Rinit-Ron)/(Rhigh-Ron);          //initial voltage across capacitor
        Gxconst = mu*Ron/(D*D);             //Gx = Gxconst*Imem*window function

// Start of the analysis
if (analysis("ic"))begin                    // to reflect the initial state of the device
        V(cap) <+ initcapV ;                //initializing capacitor to initial state
        Capv = V(cap);

end else begin
        V(capgnd) <+ 0;
        I(cap) <+ ddt(V(cap));              //current contribution from cap

        //including Vthn and Vthp, to include threshold to the device
        if  ((V(mem) > Vthp) || (V(mem) < Vthn)) begin
                //adding the window function
                I(capaux) <+ Gxconst*I(mem) *(1-(pow(((2*V(cap))-1),8)));
        end

        //including the state change radiation current effect in auxiliary circuit
        I(capaux) <+ (-1) * Gxconst*I(IRad_sc)*(1-(pow(((2*V(cap))-1),8)));
        V(capgnd) <+ 0;

end     // End of the analysis
```

```
//check the boundary conditions
if(V(cap)>=1)   V(cap)<+1;
if(V(cap)<=0)    V(cap)<+0;

V(w_D) <+ V(cap);                                   //state (w/D) of the memristor
V(mem) <+ I(mem)* ((Rhigh) -( Rhigh - Ron)* V(cap));
                                    //voltage across the memristor, V(mem)= V*Roff+Emem

end                 // End of the analog
endmodule       // End of the module
```

## Appendix B – Leaky Integrate-and-Fire Neuron Circuit

```
// Verilog-A code for leaky integrate-and-fire (LIF) circuit
`include "constants.vams"
`include "disciplines.vams"
`timescale 1us / 1ns

// Take care of current blowup error
nature Current
   abstol = 1e-14 ;
        access = I ;
        units = "A" ;
        blowup = 1e12 ;
endnature

// Start of the module
module LIF_verilog_extcap(PostIn, PostVth, testout, LICcap, gnd);
input PostVth;
inout PostIn, LICcap, gnd;
output testout;

electrical PostIn, PostVth, testout,gnd, LICcap,LICaux,LICPostIn,firesource ;
branch (PostIn,LICaux) LICswitch;
branch (LICaux,LICcap) LICcharging;
branch (LICcap,gnd) LICdischarging;

        // LIF circuit parameters
parameter real Rcharging = 10e9 ;           // charging resistance
parameter real Rdischarging = 200e9 ;       // discharging resistance
parameter real Rpostdischarge = 10e9 ;      // cap discharge during post spike
        // output pulse parameters
parameter real pulse_width = 10e-3 ;        // output pulse width
parameter real pulse_max_amp = 5 ;          // maximum output pulse V
        // circuit connecting and disconnecting parameters
parameter real Ron = 0 ;                    // connection valid, current flowing
parameter real Roff = 1e300;                // connection invalid, no current flowing

real state, tfire, t, Rfire, LICdischarging_R, LICswitch_R, V_fire, charging_timecont,
discharging_timecont, chargingstart_starttime, charging, discharging, charging_amp,
discharging_amp, discharging_endtime;       //variables used

// Start of the analog
analog begin
        charging_timecont = 0.03*pulse_width;           // charging constant
        discharging_timecont = 0.4*pulse_width;         // discharging constant
        chargingstart_starttime = 0.05*pulse_width;     // charging start time
```

```
        discharging_endtime = 0.75*pulse_width;          // discharging end time
        charging = exp(-chargingstart_starttime/charging_timecont);
        discharging = exp(-discharging_endtime/discharging_timecont);
        charging_amp = pulse_max_amp;                    // charging max voltage
        discharging_amp = pulse_max_amp*0.25;            // discharging max voltage

// Start of the analysis
if (analysis("ic"))begin
        state = 0;
        LICdischarging_R = Roff;
        LICswitch_R = Ron;
        V_fire = 0;

end else begin
        V(LICPostIn) <+ V(PostIn);                       //separate circuit and LIF circuit
        V(LICswitch) <+ I(LICswitch)*LICswitch_R;        //(dis)connect LIC circuit
        V(LICcharging) <+ I(LICcharging)*Rcharging;      //charges the LIF capacitor
        V(LICdischarging) <+ I(LICdischarging)*LICdischarging_R;
                                                         //discharges the LIF capacitor

//if vcap < vth, post-synaptic neuron is not firing
        if  (( V(LICcap) < V(PostVth)) && (state == 0))begin
                tfire = $realtime;
                LICswitch_R = Ron;                       //connect LIC circuit
                if (V(PostIn) < V(LICcap)) begin
                        LICdischarging_R = Rdischarging; //turn on cap discharging
                 LICswitch_R = Roff;                     //disconnect LIC circuit
                end
        end

//if vcap > vth, post-synaptic neuron starts firing
        else begin
                LICdischarging_R = Rpostdischarge;       //turn on cap discharging
                LICswitch_R = Roff;                      //disconnect LIC circuit
                State = 1;                               //set state to 1 for firing
                T = $realtime-tfire;                     //start timer for pulse width

        //start of the LIF spike
                if (t<= (pulse_width * 0.05)) begin    //generate potentiation part of the spike
                        V_fire = charging_amp *(t/(pulse_width * 0.05));
                end else if ((t > (pulse_width * 0.05)) && (t <= (pulse_width * 0.8))) begin
                                                         //generate depression part of the spike
                        V_fire = discharging_amp * (t - (pulse_width * 0.8))/(pulse_width * 0.75);
                end else begin
                        V_fire = 0;
                        state = 0;                       //set state to 0 for not firing
```

```
                LICdischarging_R = Roff;        //turn on cap discharging
                LICswitch_R = Ron;              //turn on LIC switch
            end     //end of LIF spike

            V(PostIn) <+ V_fire;        //initialize input terminal voltage  to V_fire

        end     //post-synaptic neuron ends firing

end     // End of the analysis

V(testout) <+ V(LICPostIn) ;            //test terminal voltage, for circuit check

end             // End of the analog
endmodule       // End of the module
```